

MAGELLAN SPECTROSCOPY OF LOW-REDSHIFT ACTIVE GALACTIC NUCLEI

LUIS C. HO¹ AND MINJIN KIM^{1,2}

To appear in The Astrophysical Journal Supplement Series.

ABSTRACT

We present an atlas of moderate-resolution ($R \approx 1200 - 1600$) optical spectra of 94 low-redshift ($z \lesssim 0.5$) active galactic nuclei taken with the Magellan 6.5 m Clay Telescope. The spectra mostly cover the rest-frame region $\sim 3600 - 6000 \text{ \AA}$. All the objects have preexisting *Hubble Space Telescope* imaging, and they were chosen as part of an ongoing program to investigate the relationship between black hole mass and their host galaxy properties. A significant fraction of the sample has no previous quantitative spectroscopic measurements in the literature. We perform spectral decomposition of the spectra and present detailed fits and basic measurements of several commonly used broad and narrow emission lines, including [O II] $\lambda 3727$, He II $\lambda 4686$, H β , and [O III] $\lambda \lambda 4959, 5007$. Eight of the objects are narrow-line sources that were previously misclassified as broad-line (type 1) Seyfert galaxies; of these, five appear not to be accretion-powered.

Subject headings: black hole physics — galaxies: active — galaxies: nuclei — galaxies: Seyfert

1. INTRODUCTION

The spectral properties of active galactic nuclei (AGNs) are pertinent to many areas of astrophysics. With the recent interest in massive black holes and their apparently close connection with galaxy evolution (see Ho 2004, and references therein), there has been a resurgence of attention on AGN properties that might lead to expedient methods to estimate black hole masses for large samples of objects. A very promising technique exploits the velocity width of the broad emission lines in type 1 sources, in combination with the size of the line-emitting region estimated from the luminosity of the central source (Kaspi et al. 2005; Bentz et al. 2009), to calculate the “virial mass” of the black hole. This technique has been calibrated for local AGNs using the H β (Kaspi et al. 2000) and H α (Greene & Ho 2005b) lines, and for higher redshift sources using ultraviolet lines (C IV $\lambda 1549$: Vestergaard 2002; Mg II $\lambda 2800$: McLure & Jarvis 2002). At the same time, the characteristics of the narrow emission lines themselves provide useful clues on the impact of AGN activity on certain aspects of the host galaxy (e.g., Netzer et al. 2004; Ho 2005; Kim et al. 2006).

This paper presents an atlas of moderate-resolution optical spectra of 94 low-redshift ($z \lesssim 0.5$), mostly broad-line (type 1) AGNs. The spectra have relatively high signal-to-noise ratios (S/N) and moderate resolution ($R = \lambda/\Delta\lambda \approx 1200 - 1600$), covering predominantly the rest-frame region $\sim 3600 - 6000 \text{ \AA}$. The observations were taken as part of an ongoing program to investigate the relationship between active black holes and their host galaxies. The ground-based, optical spectra provide the necessary material to estimate black hole masses, and existing images in the *Hubble Space Telescope* (HST) data archives give details on the host galaxy morphologies and structural parameters (for initial results, see Kim et al. 2007, 2008). Although many of the AGNs are bright, well-known sources, most of them do not have reliable, modern spectra. Of those that do, the published spectra often have highly heterogeneous quality or were analyzed in a manner inadequate for our purposes. The majority of the sample, in fact, was chosen to overlap with the AGNs selected from the *Einstein Observatory* Extended

Medium-Sensitivity Survey (EMSS; Gioia et al. 1990), an unbiased subset of which was uniformly surveyed with *HST* by Schade et al. (2000). Schade et al. objects constitute an important component of our ongoing host galaxy investigations. The original optical classifications of the EMSS AGNs were based on the spectroscopy of Stocke et al. (1991), but these authors did not publish the actual spectra, nor did they present quantitative analysis of them. We have therefore decided to reobserve as many of the objects as possible from the list of Schade et al. (2000); of the 76 objects in their sample, we observed 61 (80%). When time permitted, we also observed additional targets from the *HST* studies of low-redshift quasars by Hamilton et al. (2002) and Dunlop et al. (2003) because we also draw heavily on these samples. Some of these brighter objects already have good-quality spectra in the literature (e.g., Boroson & Green 1992; Marziani et al. 2003), but we reobserved them anyway for the sake of homogeneity.

This paper is organized as follows. Section 2 describes the observations and data reductions. Section 3 presents our method of spectral decomposition and the resulting measurements. The spectral atlas is shown in Section 4. Section 5 provides a brief summary. Distance-dependent quantities are calculated assuming the following cosmological parameters: $H_0 = 71 \text{ km s}^{-1} \text{ Mpc}^{-1}$, $\Omega_m = 0.27$, and $\Omega_\Lambda = 0.75$ (Spergel et al. 2003).

2. OBSERVATIONS AND DATA REDUCTIONS

The observations were obtained with the Magellan 6.5 m Clay Telescope on three observing runs in 23–28 February 2004, 14–18 September 2004, and 7–10 March 2005. Table 1 gives a log of the observations. The data were acquired as part of a backup program for a project that required exceptionally good seeing. We turned to the AGNs whenever the seeing conditions deteriorated to $\gtrsim 1''$, which is considered relatively poor by the standards of Las Campanas Observatory.

During the two 2004 observing runs, we used the now-retired Boller & Chivens (B&C) long-slit (length $2'$) spectrograph equipped with a 2048×515 Marconi chip. The $13.5 \mu\text{m}$ pixels project to a scale of $0''.25$. With a slit width of $0''.75$, the

¹The Observatories of the Carnegie Institution for Science, 813 Santa Barbara Street, Pasadena, CA 91101; lho@obs.carnegiescience.edu

²Department of Physics and Astronomy, Frontier Physics Research Division, Seoul National University, Seoul, Korea; mjkim@astro.snu.ac.kr

TABLE 1
SAMPLE AND OBSERVATION LOG

Name	Alternate Name	z	f_ν	$\log \nu$	A_B	Spect.	Date	Exp.	Airmass
(1)	(2)	(3)	(mJy) (4)	(Hz) (5)	(mag) (6)	(7)	(UT) (8)	(s) (9)	(10)
3C 47	PKS 0133+20	0.42516±0.000012	0.23	14.83	0.264	B&C	20 Sep. 2004	2700	1.58
3C 48	4C +32.08	0.36745±0.000068	0.96	14.83	0.188	B&C	19 Sep. 2004	1800	2.17
3C 59	4C +29.06	0.10972±0.000010	1.40	14.74	0.275	B&C	19 Sep. 2004	2700	1.93
3C 93	PKS 0340+04	0.35712±0.000009	0.17	14.83	1.046	B&C	20 Sep. 2004	2600	1.22
3C 206	PKS 0837-12	0.19787±0.000009	0.59	14.85	0.194	B&C	26 Feb. 2004	3600	1.07
[HB89] 0205+024	MRK 586	0.15554±0.000437	2.04	14.85	0.127	B&C	19 Sep. 2004	1800	1.30
[HB89] 0257+024	US 3498	0.11337±0.000021	0.64	14.81	0.363	B&C	20 Sep. 2004	1800	1.24
[HB89] 0316-346	1H 0311-348	0.26619±0.000321	3.33	14.83	0.073	B&C	26 Feb. 2004	1200	1.27
[HB89] 0450-299	IRAS 04505-2958	0.28593±0.000049	1.40	14.74	0.064	B&C	19 Sep. 2004	1800	1.01
[HB89] 0736+017	PKS 0736+01	0.18941±0.000009	1.00	14.85	0.549	B&C	24 Feb. 2004	1800	1.18
[HB89] 1635+119	MC2 1635+119	0.14748±0.000037	0.51	14.79	0.223	B&C	17 Sep. 2004	1800	1.72
[HB89] 2201+315	4C +31.63	0.29474±0.000009	2.69	14.85	0.534	B&C	20 Sep. 2004	1800	2.17
[HB89] 2344+184	2MASX J23472568+1844502	0.13668±0.000102	1.57	14.74	0.339	B&C	17 Sep. 2004	1800	1.95
HE 1029-1401	RBS 880	0.08582±0.000009	20.40	14.84	0.288	B&C	26 Feb. 2004	8400	1.06
LBQS 0020+0018	SDSS J002311.05+003517.4	0.42208±0.000047	0.08	14.79	0.105	B&C	20 Sep. 2004	2700	1.56
LBQS 0021-0301		0.42053±0.000043	0.13	14.81	0.137	B&C	20 Sep. 2004	2700	1.28
LBQS 2214-1903		0.39657±0.000089	0.23	14.81	0.118	B&C	18 Sep. 2004	2700	1.02
MS 0007.1-0231	2MASX J00093952-0214375	0.08558±0.000137	0.51	14.81	0.159	B&C	17 Sep. 2004	1800	1.33
MS 0039.0-0145	2MASX J00413676-0129134	0.11115±0.000018	0.10	14.81	0.103	B&C	17 Sep. 2004	1800	1.33
MS 0048.8+2907	UGC 524	0.03616±0.000094	7.40	14.83	0.272	B&C	16 Sep. 2004	300	1.99
MS 0100.6+0205	UM 301	0.39357±0.000043	0.42	14.81	0.090	B&C	19 Sep. 2004	2700	1.60
MS 0111.9-0132	[HB89] 0111-015	0.11835±0.000210	0.11	14.81	0.327	B&C	17 Sep. 2004	1800	1.23
MS 0135.4+0256		0.15020±0.000046	0.25	14.74	0.211	B&C	17 Sep. 2004	1800	1.21
MS 0144.2-0055	SDSS J014644.82-004043.2	0.08279±0.000029	0.19	14.81	0.165	B&C	17 Sep. 2004	1200	1.16
MS 0244.8+1928	[HB89] 0244+194	0.17489±0.000088	0.78	14.74	0.479	B&C	19 Sep. 2004	1800	1.57
MS 0321.5-6657	2MASX J03221410-6647062	0.09458±0.000082	1.72	14.74	0.194	B&C	16 Sep. 2004	1800	1.27
MS 0330.8+0606	2MASX J03333242+0616420	0.10610±0.000019	0.30	14.74	1.072	B&C	17 Sep. 2004	1800	1.24
MS 0340.3+0455	2MASX J03425520+0505089	0.09600±0.000252	0.28	14.74	1.108	B&C	17 Sep. 2004	1800	1.21
MS 0412.4-0802	IRAS 04124-0803	0.03823±0.000009	0.68	14.81	0.363	B&C	16 Sep. 2004	90	1.07
MS 0444.9-1000	2MASX J04471629-0955348	0.09494±0.000026	0.36	14.74	0.293	B&C	17 Sep. 2004	1800	1.07
MS 0457.9+0141	2MASX J05003243+0146143	0.12731±0.000010	0.29	14.74	0.378	B&C	16 Sep. 2004	1800	1.20
MS 0516.6-4609	2MASX J05180325-4606130	0.04817±0.000025	0.96	14.81	0.129	B&C	28 Feb. 2004	1800	1.17
MS 0801.9+2129	SDSS J080452.73+212050.2	0.12468±0.000069	0.75	14.79	0.285	B&C	27 Feb. 2004	1800	1.57
MS 0841.7+1628	SDSS J084428.69+161654.1	0.14908±0.000089	0.10	14.79	0.103	LDSS3	08 Mar. 2005	1800	1.52
MS 0842.7-0720	2MASX J08451026-0732051	0.10399±0.000044	0.59	14.74	0.147	B&C	28 Feb. 2004	1800	1.14
MS 0844.9+1836	SDSS J084748.28+182439.9	0.08540±0.000954	0.31	14.79	0.103	B&C	28 Feb. 2004	1800	1.50
MS 0849.5+0805	SDSS J085215.11+075336.1	0.06230±0.000073	1.39	14.79	0.213	LDSS3	08 Mar. 2005	941	1.29
MS 0904.4-1505	2MASX J09064794-1517441	0.05460±0.000051	0.84	14.74	0.288	B&C	28 Feb. 2004	1800	1.06
MS 0905.6-0817	2MASX J09080549-0829458	0.07085±0.000010	0.72	14.74	0.235	B&C	28 Feb. 2004	1800	1.07
MS 0942.8+0950	SDSS J094529.37+093610.4	0.01334±0.000014	0.61	14.79	0.107	LDSS3	08 Mar. 2005	1800	1.32
MS 0944.1+1333	SDSS J094651.95+132025.9	0.13194±0.000009	0.03	14.79	0.172	LDSS3	09 Mar. 2005	1800	1.36
MS 1058.8+1003	SDSS J110126.47+094720.0	0.02692±0.000238	0.85	14.79	0.133	LDSS3	09 Mar. 2005	1200	1.32
MS 1108.3+3530	SDSS J111104.81+351350.9	0.06073±0.000043	0.30	14.79	0.091	LDSS3	09 Mar. 2005	1502	2.29
MS 1110.3+2210	SDSS J111258.29+215434.0	0.02938±0.000482	0.18	14.79	0.077	LDSS3	09 Mar. 2005	1800	1.59
MS 1114.4+1801		0.09187±0.000039	0.90	14.74	0.083	LDSS3	09 Mar. 2005	1800	1.59
MS 1136.5+3413	SDSS J113913.92+335551.2	0.03234±0.000184	0.53	14.79	0.082	LDSS3	09 Mar. 2005	1800	2.22
MS 1139.7+1040	SDSS J114216.79+102339.2	0.15084±0.000057	0.17	14.79	0.223	B&C	28 Feb. 2004	1800	1.29
MS 1143.5-0411	2MASX J11460396-0428013	0.13393±0.000064	0.28	14.81	0.086	B&C	28 Feb. 2004	1800	1.12
MS 1158.6-0323	MRK 1310	0.01956±0.000012	1.56	14.79	0.133	B&C	28 Feb. 2004	900	1.17
MS 1200.1-0330	2MASX J12024536-0347215	0.06452±0.000111	0.52	14.81	0.135	LDSS3	08 Mar. 2005	1800	1.13
MS 1217.0+0700	SDSS J121930.87+064334.4	0.08058±0.000114	0.51	14.79	0.086	B&C	28 Feb. 2004	1800	1.23
MS 1220.9+1601	SDSS J122330.79+154507.4	0.08069±0.000049	0.18	14.79	0.114	LDSS3	08 Mar. 2005	1800	1.42

TABLE 1—*Continued*

Name	Alternate Name	z	f_ν (mJy)	$\log \nu$ (Hz)	A_B (mag)	Spect.	Date (UT)	Exp. (s)	Airmass
(1)	(2)	(3)	(4)	(5)	(6)	(7)	(8)	(9)	(10)
MS 1232.4+1550	IC 3528	0.04612±0.000027	0.47	14.79	0.145	B&C	28 Feb. 2004	1800	1.40
MS 1239.2+3219	SDSS J124145.71+320256.2	0.05011±0.000013	0.21	14.79	0.069	LDSS3	09 Mar. 2005	1278	2.10
MS 1242.2+1632	2MASXi J1244415+161610	0.08776±0.000009	0.50	14.74	0.139	B&C	28 Feb. 2004	1800	1.43
MS 1306.1−0115	SDSS J130845.68−013053.9	0.11046±0.000012	0.19	14.79	0.092	LDSS3	08 Mar. 2005	1800	1.14
MS 1322.3+2925	SDSS J132438.73+291012.1	0.07239±0.000171	0.17	14.79	0.062	LDSS3	08 Mar. 2005	1800	1.89
MS 1334.6+0351	SDSS J133709.70+033556.1	0.13566±0.000158	0.08	14.79	0.106	LDSS3	08 Mar. 2005	1800	1.19
MS 1335.1−3128		0.08131±0.000114	0.09	14.74	0.232	LDSS3	09 Mar. 2005	1800	1.01
MS 1414.0+0130	SDSS J141639.91+011629.4	0.13804±0.000811	0.10	14.79	0.153	LDSS3	08 Mar. 2005	1800	1.17
MS 1414.9+1337	SDSS J141722.79+132330.1	0.08849±0.000441	0.10	14.79	0.100	LDSS3	08 Mar. 2005	1800	1.43
MS 1416.3−1257	PG 1416−129	0.12894±0.000012	1.15	14.83	0.404	B&C	28 Feb. 2004	900	1.05
MS 1426.5+0130	PG 1426+015	0.08657±0.000038	6.02	14.79	0.137	B&C	28 Feb. 2004	1800	1.16
MS 1455.7+2121	SDSS J145759.94+210955.4	0.08301±0.000032	0.28	14.79	0.191	LDSS3	08 Mar. 2005	900	1.63
MS 1456.4+2147	SDSS J145842.74+213609.9	0.06354±0.000018	0.65	14.79	0.175	B&C	28 Feb. 2004	1100	1.57
MS 1519.8−0633	[HB89] 1519−065	0.08296±0.000202	3.95	14.74	0.415	B&C	26 Feb. 2004	1800	1.43
MS 1545.3+0305	SDSS J154751.93+025550.8	0.09822±0.000030	0.34	14.79	0.491	B&C	28 Feb. 2004	900	1.23
MS 1549.8+2022	[HB89] 1549+203	0.25186±0.000315	0.40	14.74	0.230	B&C	19 Sep. 2004	1800	2.31
MS 1846.5−7857	ESO 025−G002	0.02916±0.000018	6.39	14.83	0.695	B&C	15 Sep. 2004	900	1.55
MS 2039.5−0107	SDSS J204205.65−005718.8	0.14341±0.000018	0.11	14.79	0.264	B&C	15 Sep. 2004	1800	1.15
MS 2128.3+0349	2MASX J21305288+0402300	0.08612±0.000012	1.05	14.74	0.219	B&C	16 Sep. 2004	1800	1.24
MS 2141.2+1730	OX 169	0.21074±0.000009	1.86	14.73	0.478	B&C	19 Sep. 2004	1800	1.84
MS 2144.9−2012	2MASX J21474454−1958114	0.10281±0.000034	0.27	14.81	0.153	B&C	15 Sep. 2004	1800	1.39
MS 2159.5−5713	2MASX J22025520−5659376	0.08388±0.000019	0.41	14.81	0.114	B&C	16 Sep. 2004	1800	1.24
MS 2210.2+1827	2MASX J22123700+1842281	0.07838±0.000110	0.73	14.74	0.209	B&C	16 Sep. 2004	1800	1.52
MS 2215.2−0347	[HB89] 2215−037	0.24099±0.000079	0.47	14.74	0.455	B&C	18 Sep. 2004	1800	1.51
MS 2348.3+3250		0.09183±0.000019	0.25	14.74	0.235	B&C	16 Sep. 2004	1800	2.14
MS 2348.6+1956	2MASX J23511391+2013464	0.04295±0.000114	2.24	14.83	0.326	B&C	16 Sep. 2004	1800	1.58
PG 0043+039	[HB89] 0043+039	0.38512±0.000009	2.64	14.87	0.090	B&C	20 Sep. 2004	1800	1.30
PG 0050+124	I Zw 1	0.05890±0.000021	6.20	14.83	0.279	B&C	16 Sep. 2004	300	1.47
PG 0052+251	[HB89] 0052+251	0.15445±0.000009	2.17	14.79	0.205	B&C	20 Sep. 2004	1200	1.80
PG 0157+001	MRK 1014	0.16311±0.000016	2.01	14.79	0.125	B&C	19 Sep. 2004	1800	1.34
PG 1012+008	SDSS J101454.90+003337.3	0.18674±0.000129	1.24	14.79	0.151	B&C	27 Feb. 2004	2400	1.18
PG 2349−014	SDSS J235156.12−010913.3	0.17416±0.000026	1.78	14.79	0.119	B&C	17 Sep. 2004	1800	2.03
PHL 909	SDSS J005709.92+144610.1	0.17178±0.000274	1.26	14.79	0.196	B&C	19 Sep. 2004	2700	1.61
PHL 1093	PKS 0137+012	0.26168±0.000011	0.79	14.83	0.125	B&C	20 Sep. 2004	1800	1.24
PHL 6113	PKS 2355−082	0.21098±0.000018	0.36	14.74	0.173	B&C	19 Sep. 2004	2700	1.35
PKS 0021−29	MRC 0022−297	0.40645±0.000020	0.09	14.74	0.092	B&C	18 Sep. 2004	2700	1.58
PKS 0202−76	[HB89] 0202−765	0.38939±0.000024	0.71	14.74	0.219	B&C	18 Sep. 2004	1800	1.85
PKS 0312−77	[HB89] 0312−770	0.22519±0.000009	1.31	14.74	0.417	B&C	19 Sep. 2004	1800	1.49
PKS 1020−103	[HB89] 1020−103	0.19662±0.000012	1.29	14.74	0.199	LDSS3	09 Mar. 2005	1200	1.12
PKS 1548+114	MRC 1548+114	0.43598±0.000018	0.12	14.79	0.232	B&C	18 Sep. 2004	1800	1.95
PKS 2135−14	[HB89] 2135−147	0.20047±0.000013	2.63	14.85	0.219	B&C	17 Sep. 2004	1800	1.36
PKS 2247+14	SDSS J225025.34+141952.0	0.23463±0.000024	0.55	14.79	0.218	B&C	20 Sep. 2004	1800	1.80

NOTE.— Col. (1) Name. Col. (2) Alternate name. Col. (3) Redshift, based on our own measurement of the centroid of the [O III] λ 5007 line. Col. (4) Optical flux density, taken from NED. Col. (5) Frequency of f_ν . Col. (6) Galactic extinction in the B band (Schlegel et al. 1998). Col. (7) Spectrograph. Col. (8) Date of observations. Col. (9) Total exposure time. Col. (10) Airmass.

600 lines mm^{-1} grating gave an average full-width at half maximum (FWHM) resolution of 4.2 \AA (250 km s^{-1} at 5000 \AA). The spectral resolution, as judged by the widths of the comparison arc-lamp spectra and the night sky lines, was relatively uniform across the spectrum. Two grating tilts were used in order to observe the rest-frame region of most interest to us, $4200\text{--}5750 \text{ \AA}$, which contains the diagnostically important lines of He II $\lambda 4686$, $H\beta$, [O III] $\lambda\lambda 4959, 5007$, and two of the prominent optical Fe II blends. For sources with $z \leq 0.185$, we covered the spectral range $\sim 3640\text{--}6820 \text{ \AA}$; for those with $z > 0.185$, the grating tilt was set to cover $\sim 4900\text{--}8075 \text{ \AA}$.

The 2005 run employed the Low-Dispersion Survey Spectrograph (LDSS3)³ in long-slit mode. The 4096×4096 detector has $15 \mu\text{m}$ pixels and a scale of $0''.189 \text{ pixel}^{-1}$. We cut three slit masks, each with a long slit $0''.8$ wide, which, in combination with a blue and a red volume-phase holographic grating, gave us a total of four spectral settings, each covering $\sim 2500 \text{ \AA}$. The $1090 \text{ lines mm}^{-1}$ blue grating has a spectral resolution of $\text{FWHM} = 3.2 \text{ \AA}$ (190 km s^{-1} at 5000 \AA), and the $660 \text{ lines mm}^{-1}$ red grating has a spectral resolution of $\text{FWHM} = 6.5 \text{ \AA}$ (245 km s^{-1} at 8000 \AA).

Pixel-to-pixel variations in the response of the CCD were corrected using domeflats illuminated by external quartz lamps. The B&C data show low-level fringing at wavelengths longer than $\sim 6000 \text{ \AA}$. To remove this effect, for each science image we generated a hybrid flat by combining a contemporaneous domeflat for $\lambda > 6000 \text{ \AA}$ with a high-S/N flat for shorter wavelengths derived from median-combining a large number (40) of afternoon domeflats. Bias correction was achieved by subtracting a constant count level determined from the overscan region of the chip. We took dark frames to verify that the CCDs indeed have sufficiently low dark current that it can be ignored. The spectra were wavelength-calibrated using comparison arc-lamp spectra, taken at the position of each target, of He+Ar for the B&C runs and He+Ar+Ne for the LDSS3 run. The wavelength solution is typically accurate to $\sim 0.03 \text{ \AA}$ rms.

We observed a number of bright G and K giant and subgiant stars, as well as a few A-type dwarfs, to model the host galaxy starlight (Section 3). To perform relative flux calibration, we observed spectrophotometric standard stars with nearly featureless continua—usually white dwarfs (Stone & Baldwin 1983; Baldwin & Stone 1984)—at two widely separated airmasses at the beginning and end of each night. Because of the narrowness of the slit and the (deliberately) non-optimal conditions of the observations, the absolute flux scale is not accurate. To obtain an approximate absolute flux calibration, we empirically bootstrap the observed flux scale to flux densities estimated from optical magnitudes collected from the literature (Table 1). Whenever possible, we chose literature fluxes that were taken with the smallest possible aperture in order to mimic our narrow slit width. As the literature values are quite heterogeneous, our final fluxes are only approximate, accurate perhaps to no better than a factor of ~ 2 .

Most of the observations were taken with the slit oriented at the parallactic angle to minimize slit losses from atmospheric differential refraction (Filippenko 1982). In a few cases where this was not true, and the airmass was substantial, slit losses

introduced significant distortion of the continuum shape in the blue. The total exposure time of each target varied from 90 to 3600 s, depending on the apparent brightness of the source and the prevailing weather conditions (some objects were observed under heavy cloud cover). To the extent possible, we attempted to reach a uniform minimum S/N threshold ($\sim 50\text{--}60$ per pixel in the continuum), as judged from real-time, quick-look reduction of the data. This was not always realized because of the challenging sky conditions. Multiple (long + short) exposures were taken of some objects to prevent saturation of the brightest emission lines.

We reduced the spectra following standard procedures within the IRAF⁴ package `longslit`. Prior to generating one-dimensional spectra, which uses optimal extraction (Horne 1986), we removed cosmic rays using the algorithm of van Dokkum (2001). Sky subtraction for the B&C data was performed in a straightforward manner by averaging background regions on either side of the object. However, the LDSS3 data required more extensive treatment, incorporated into the COSMOS data reduction package⁵, in order to rectify the significant curvature in the spatial direction of the images. In the end, the sky subtraction for the LDSS3 data was not fully satisfactory, and regions of the spectra near strong night sky lines were adversely affected. In most instances, this has no significant scientific impact, but in a few objects important spectral features were partly corrupted. For cosmetic purposes, in the final presentation of the spectra, we removed the small affected regions by interpolation. Finally, regions of the spectrum in long exposures that were saturated were replaced with suitably scaled portions from the shorter, unsaturated exposure.

Telluric oxygen absorption lines near 6280 \AA , 6860 \AA (the “B band”), and 7580 \AA (the “A band”) were removed by division of normalized, intrinsically featureless spectra of the standard stars. Large residuals caused by mismatches at the strong bandheads were eliminated by interpolation in the plotted spectra. The reduction procedure also corrected for continuum atmospheric extinction.

3. SPECTRAL ATLAS

Figure 1 presents the spectra for the sources, arranged in increasing alphanumeric order. Each panel shows the final spectrum, corrected for foreground Galactic extinction using the *B*-band extinctions given by Schlegel et al. (1998) and the extinction curve of Cardelli et al. (1989). We shifted the spectra to the source rest-frame using the heliocentric radial velocity determined from the centroid of the narrow core of the [O III] $\lambda 5007$ line (see Section 4), as listed in Table 1. The [O III] centroid is typically accurate to $\sim 0.13 \text{ \AA}$, or $\sim 7.8 \text{ km s}^{-1}$, consistent with independent checks from published redshifts given in the NASA/IPAC Extragalactic Database (NED). For the purposes of the presentation, a few objects [whose names are followed by “(s)”] with particularly low S/N have been smoothed with a 5-pixel boxcar. As explained in Section 2, the flux density scale is only approximate; the reader should exercise caution in using it for quantitative analysis. These spectra are available upon request from the authors.

³ Information on current Magellan instrumentation can be found at <http://www.lco.cl/lco/telescopes-information/magellan/instruments>

⁴ IRAF is distributed by the National Optical Astronomy Observatory, which is operated by the Association of Universities for Research in Astronomy (AURA) under cooperative agreement with the National Science Foundation.

⁵ <http://www.ociw.edu/Code/cosmos>

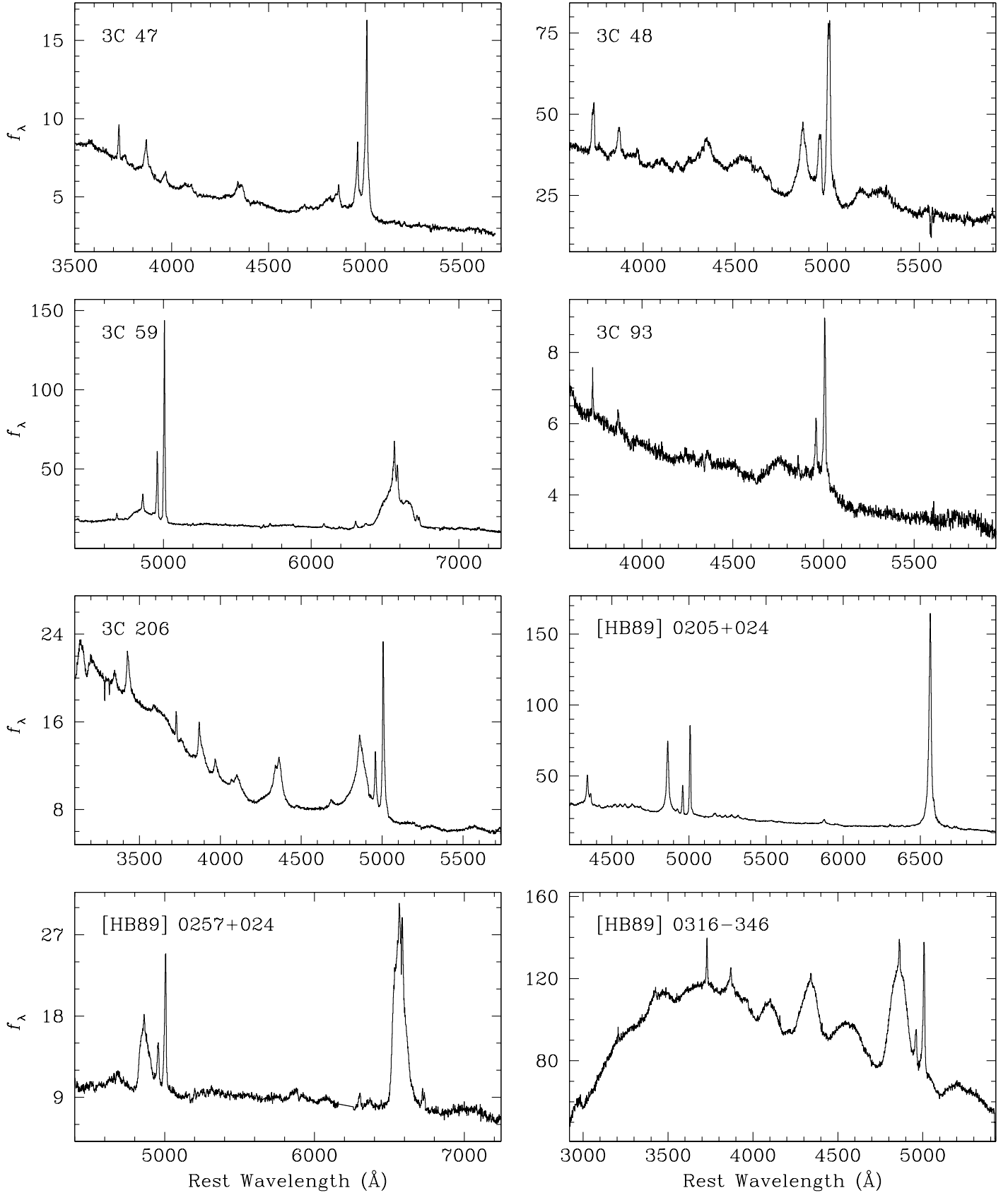


FIG. 1.— Spectral atlas. The ordinate is in units of $10^{-16} \text{ erg s}^{-1} \text{ cm}^{-2} \text{ \AA}^{-1}$. Objects marked with “(s)” were smoothed with a 5-pixel boxcar.

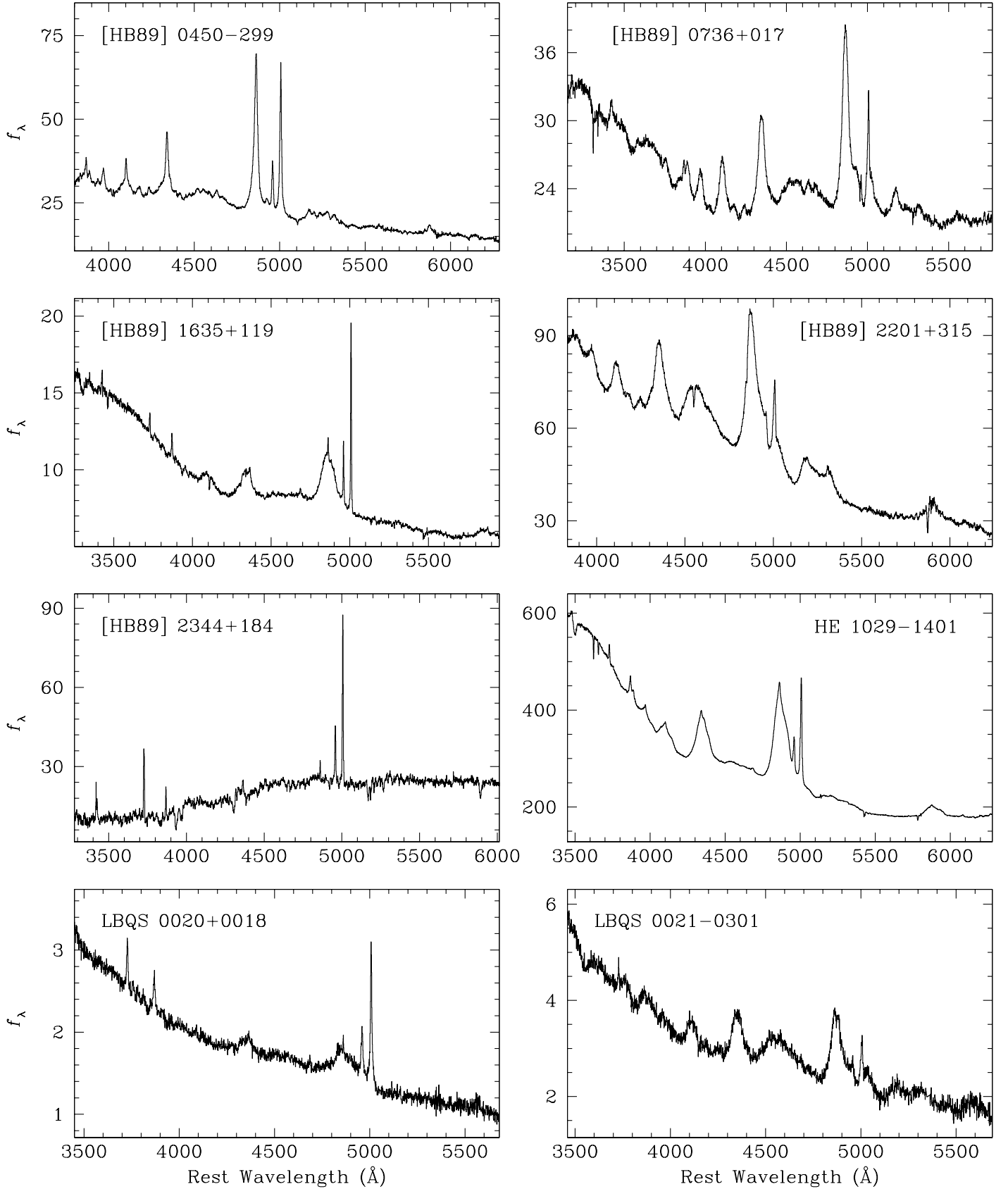


FIG. 1.— Spectral atlas. The ordinate is in units of $10^{-16} \text{ erg s}^{-1} \text{ cm}^{-2} \text{ \AA}^{-1}$. Objects marked with “(s)” were smoothed with a 5-pixel boxcar.

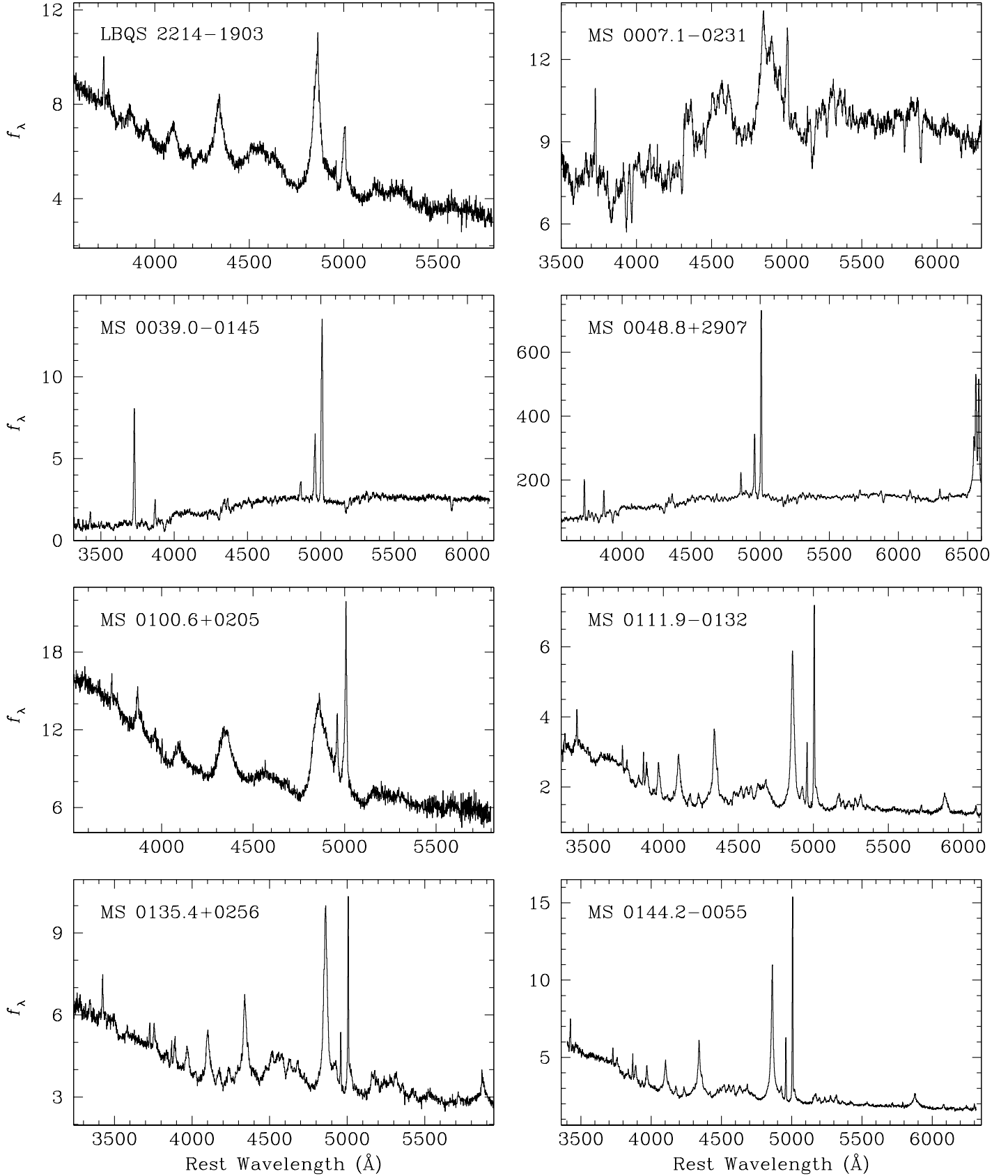


FIG. 1.— Spectral atlas. The ordinate is in units of $10^{-16} \text{ erg s}^{-1} \text{ cm}^{-2} \text{ \AA}^{-1}$. Objects marked with “(s)” were smoothed with a 5-pixel boxcar.

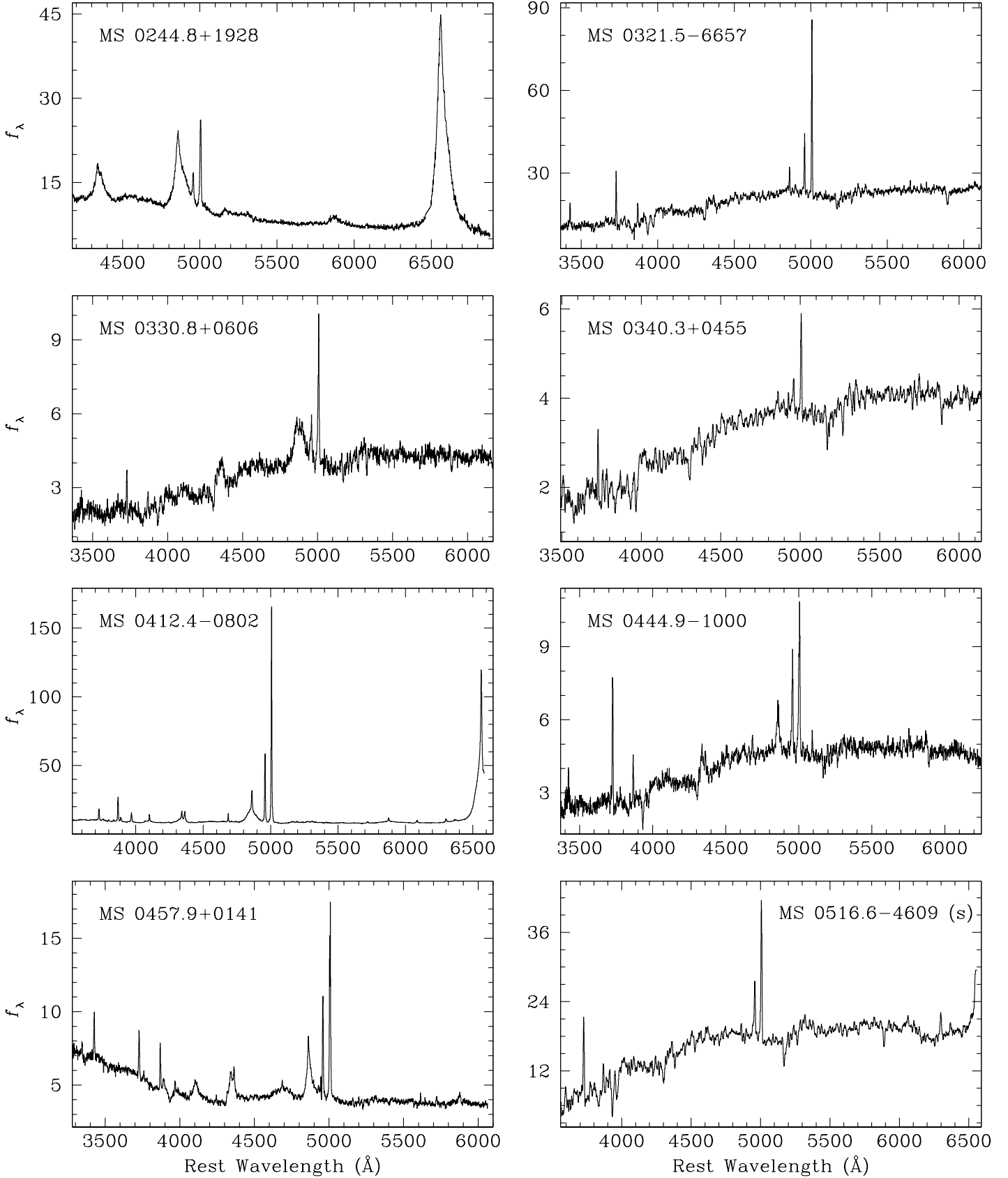


FIG. 1.— Spectral atlas. The ordinate is in units of $10^{-16} \text{ erg s}^{-1} \text{ cm}^{-2} \text{ \AA}^{-1}$. Objects marked with “(s)” were smoothed with a 5-pixel boxcar.

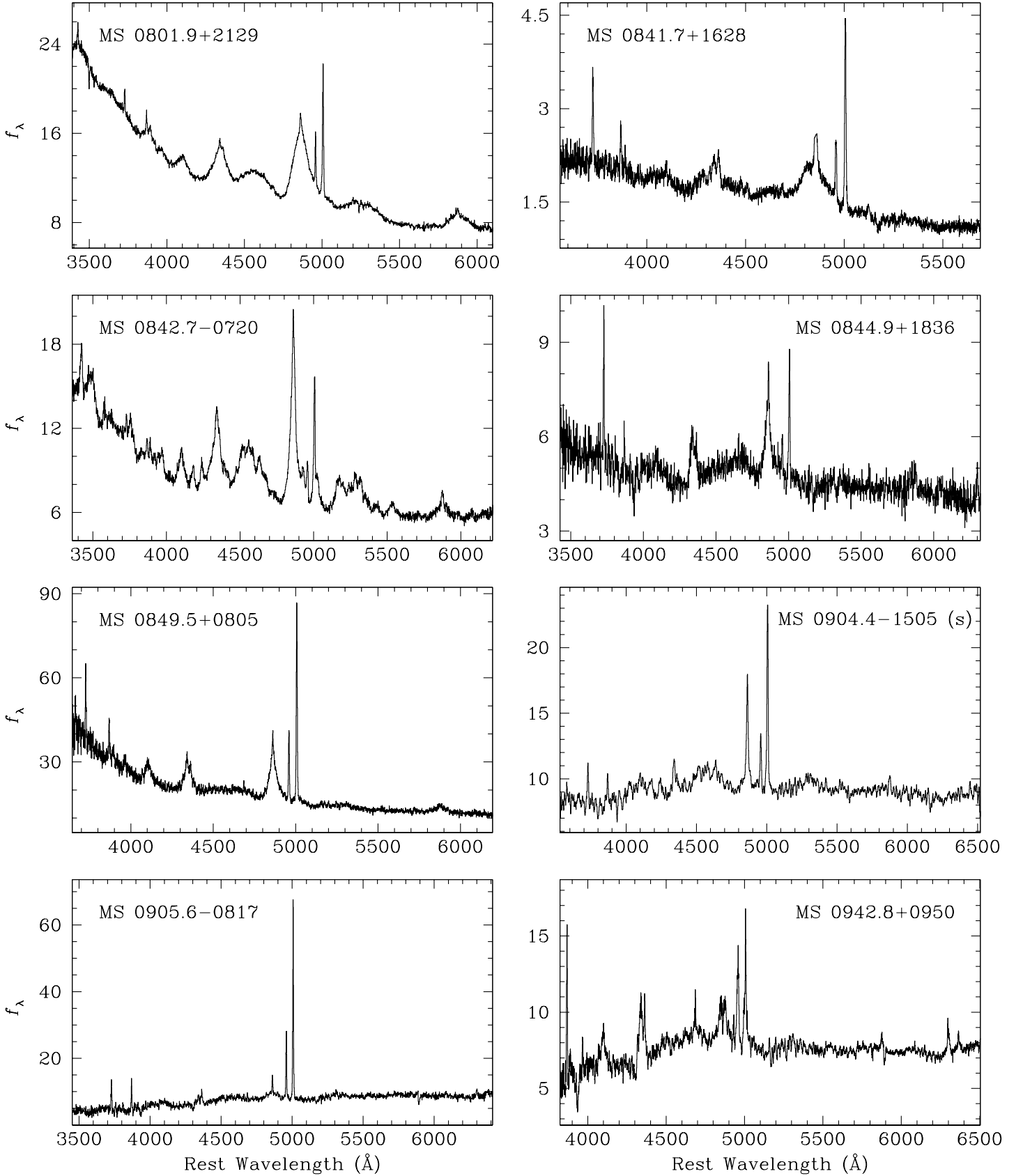


FIG. 1.— Spectral atlas. The ordinate is in units of $10^{-16} \text{ erg s}^{-1} \text{ cm}^{-2} \text{ \AA}^{-1}$. Objects marked with “(s)” were smoothed with a 5-pixel boxcar.

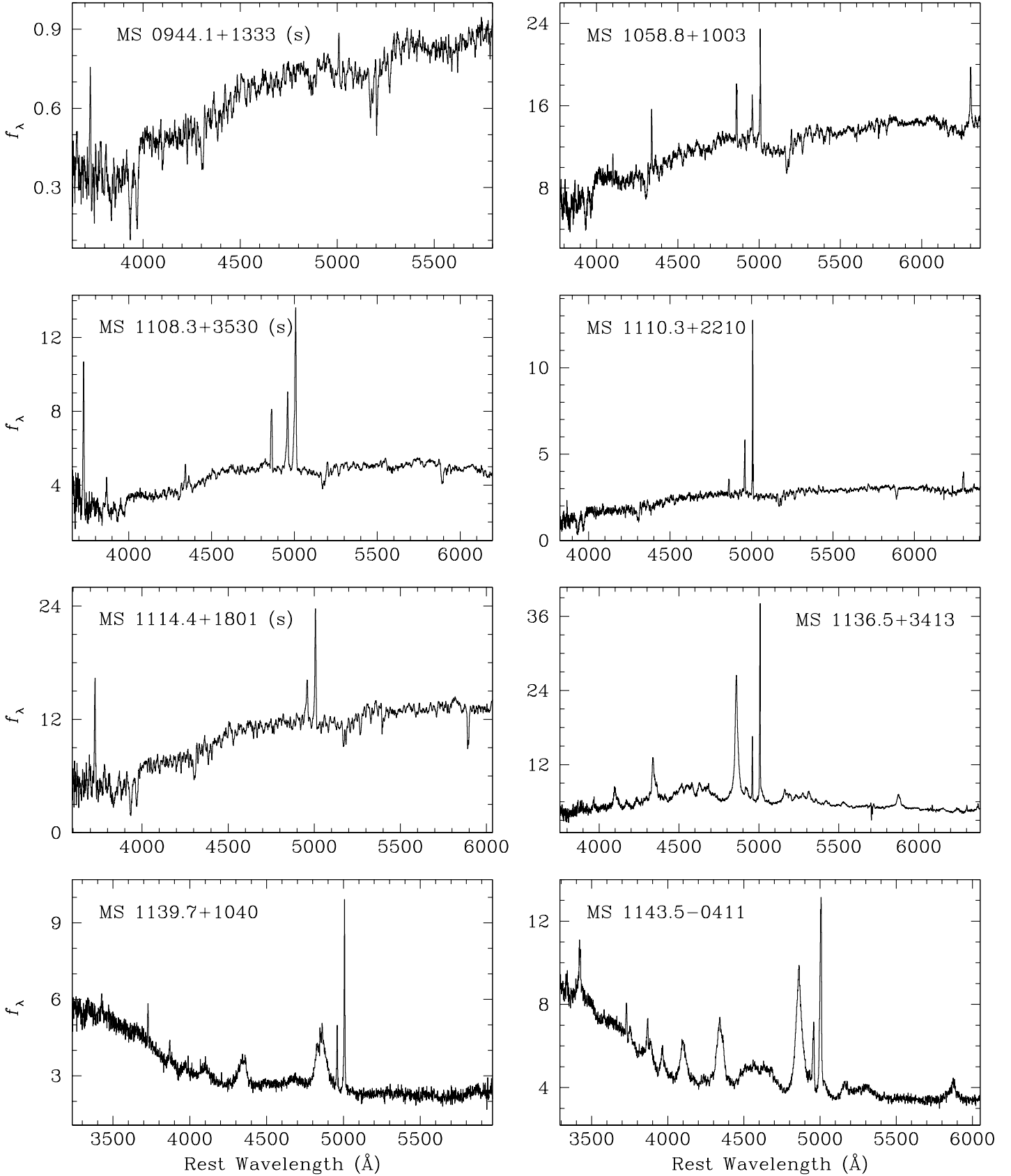


FIG. 1.— Spectral atlas. The ordinate is in units of 10^{-16} erg s^{-1} cm^{-2} \AA^{-1} . Objects marked with “(s)” were smoothed with a 5-pixel boxcar.

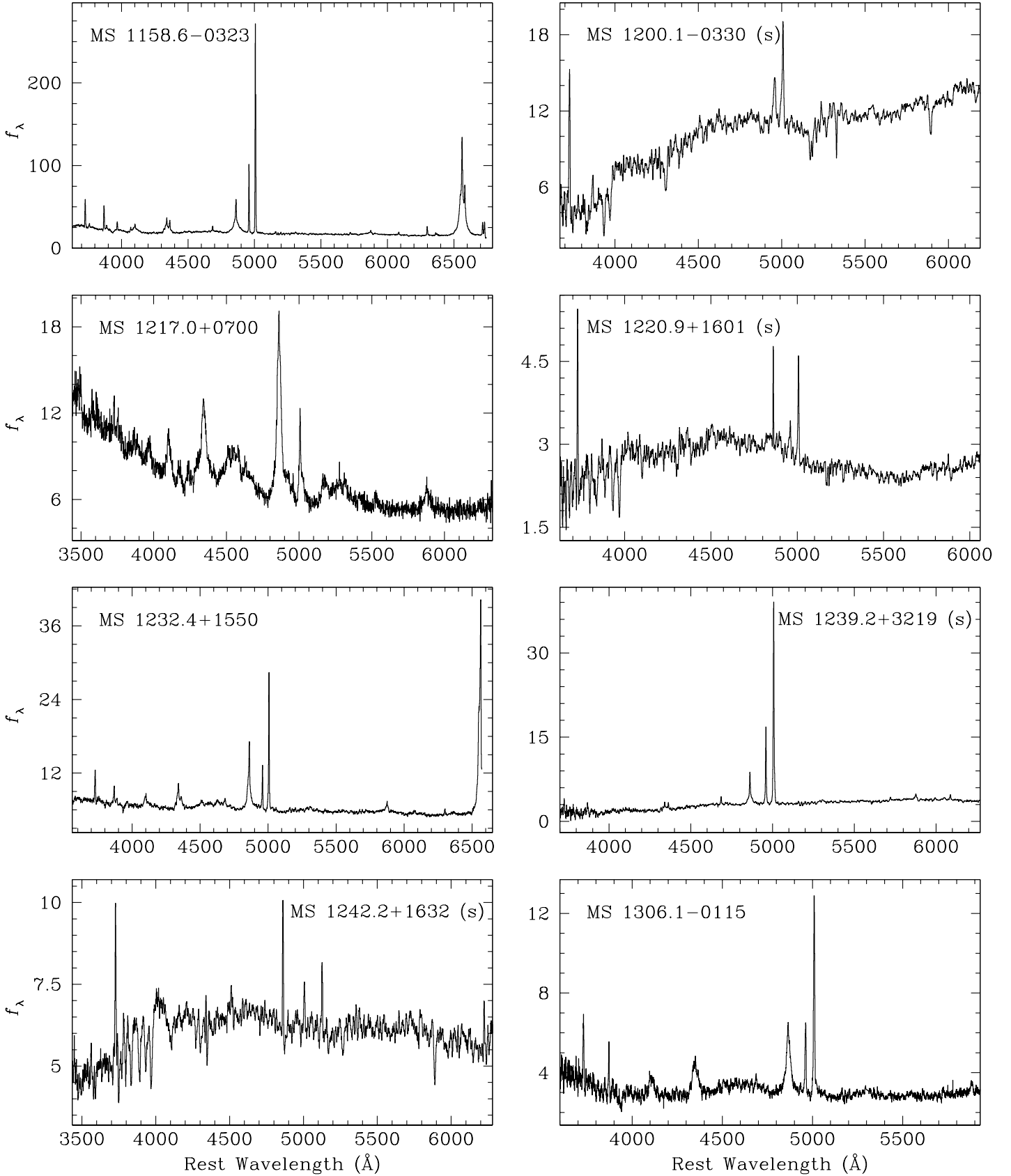


FIG. 1.— Spectral atlas. The ordinate is in units of $10^{-16} \text{ erg s}^{-1} \text{ cm}^{-2} \text{ \AA}^{-1}$. Objects marked with “(s)” were smoothed with a 5-pixel boxcar.

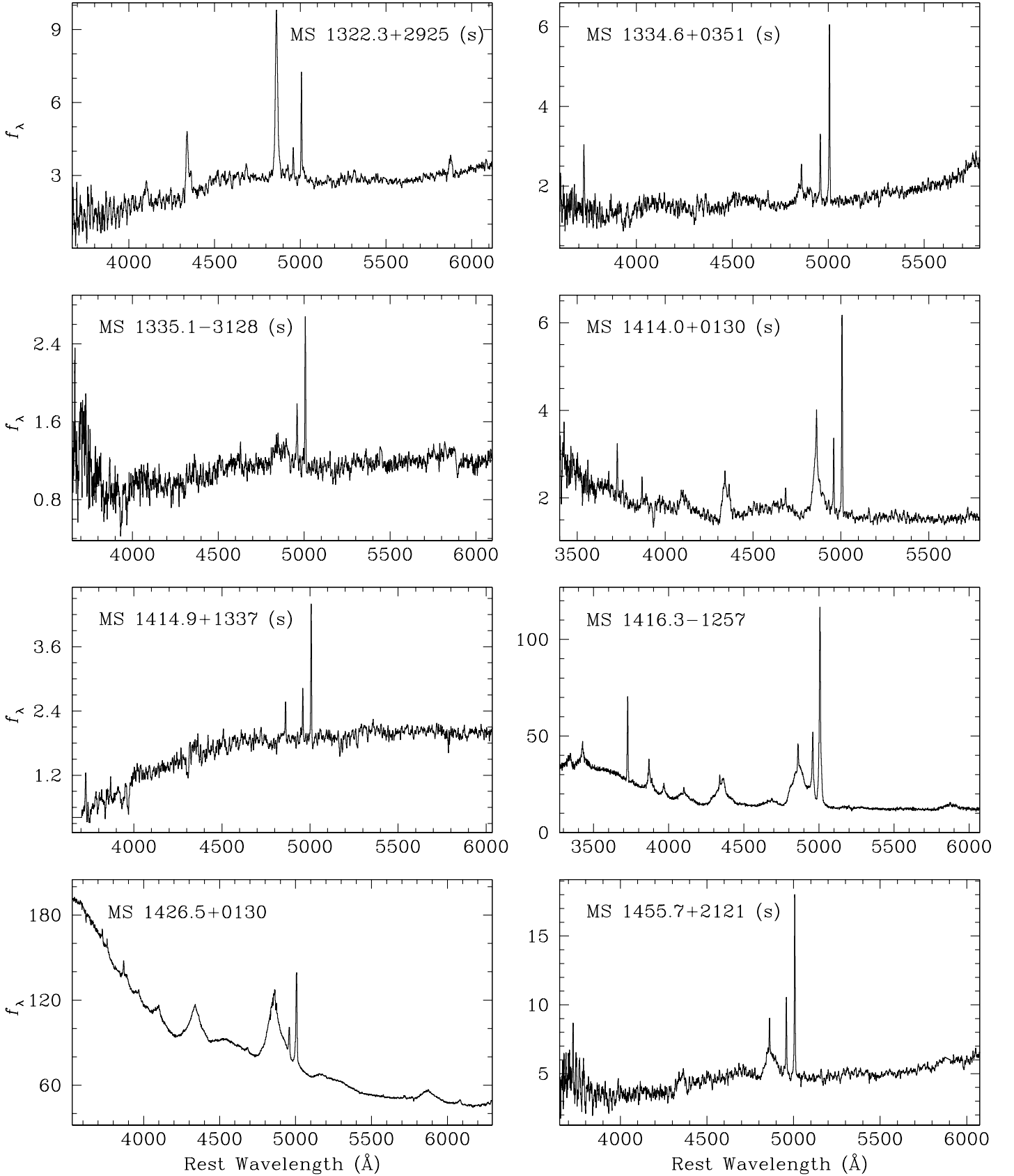


FIG. 1.— Spectral atlas. The ordinate is in units of $10^{-16} \text{ erg s}^{-1} \text{ cm}^{-2} \text{ \AA}^{-1}$. Objects marked with “(s)” were smoothed with a 5-pixel boxcar.

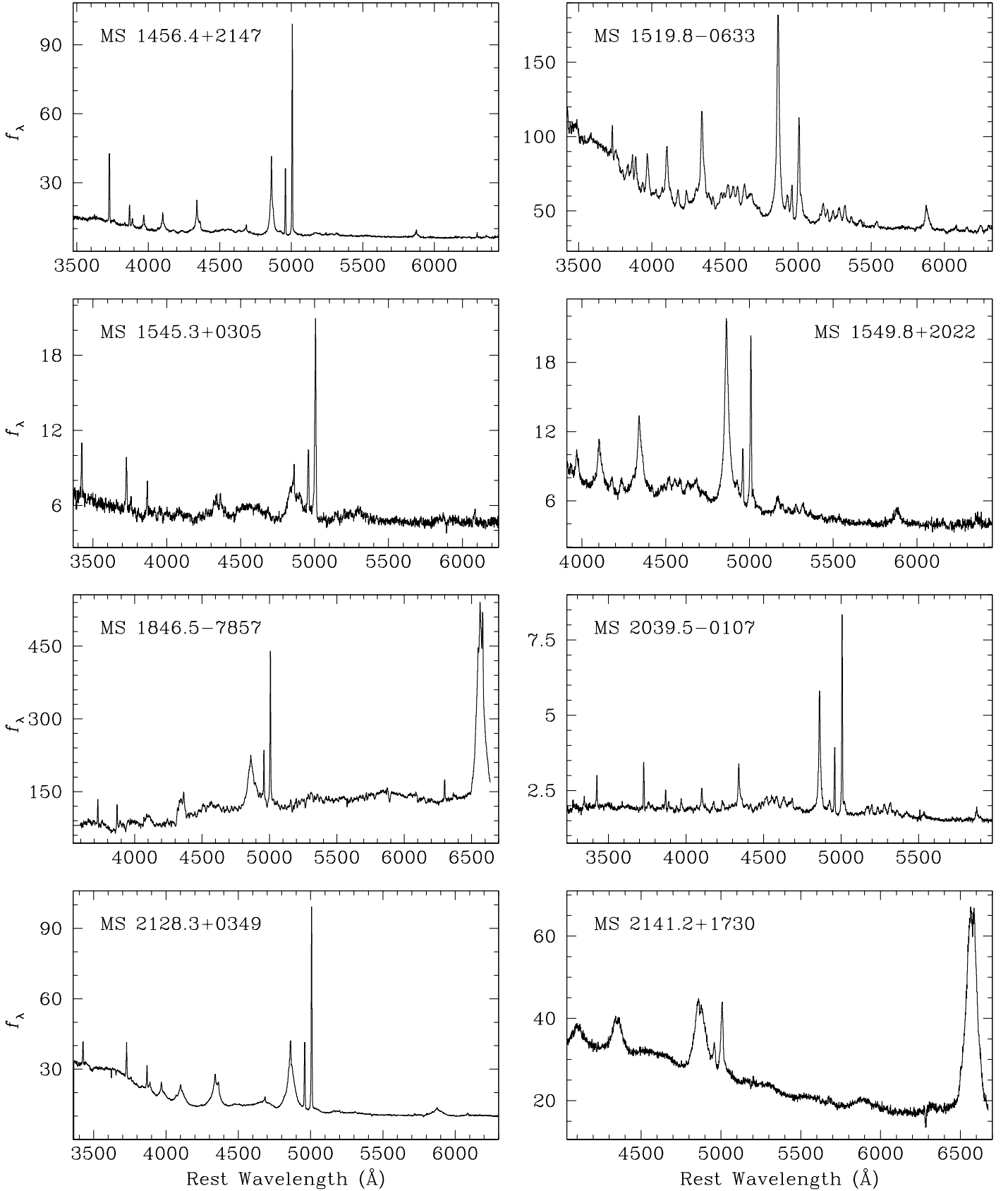


FIG. 1.— Spectral atlas. The ordinate is in units of $10^{-16} \text{ erg s}^{-1} \text{ cm}^{-2} \text{ \AA}^{-1}$. Objects marked with “(s)” were smoothed with a 5-pixel boxcar.

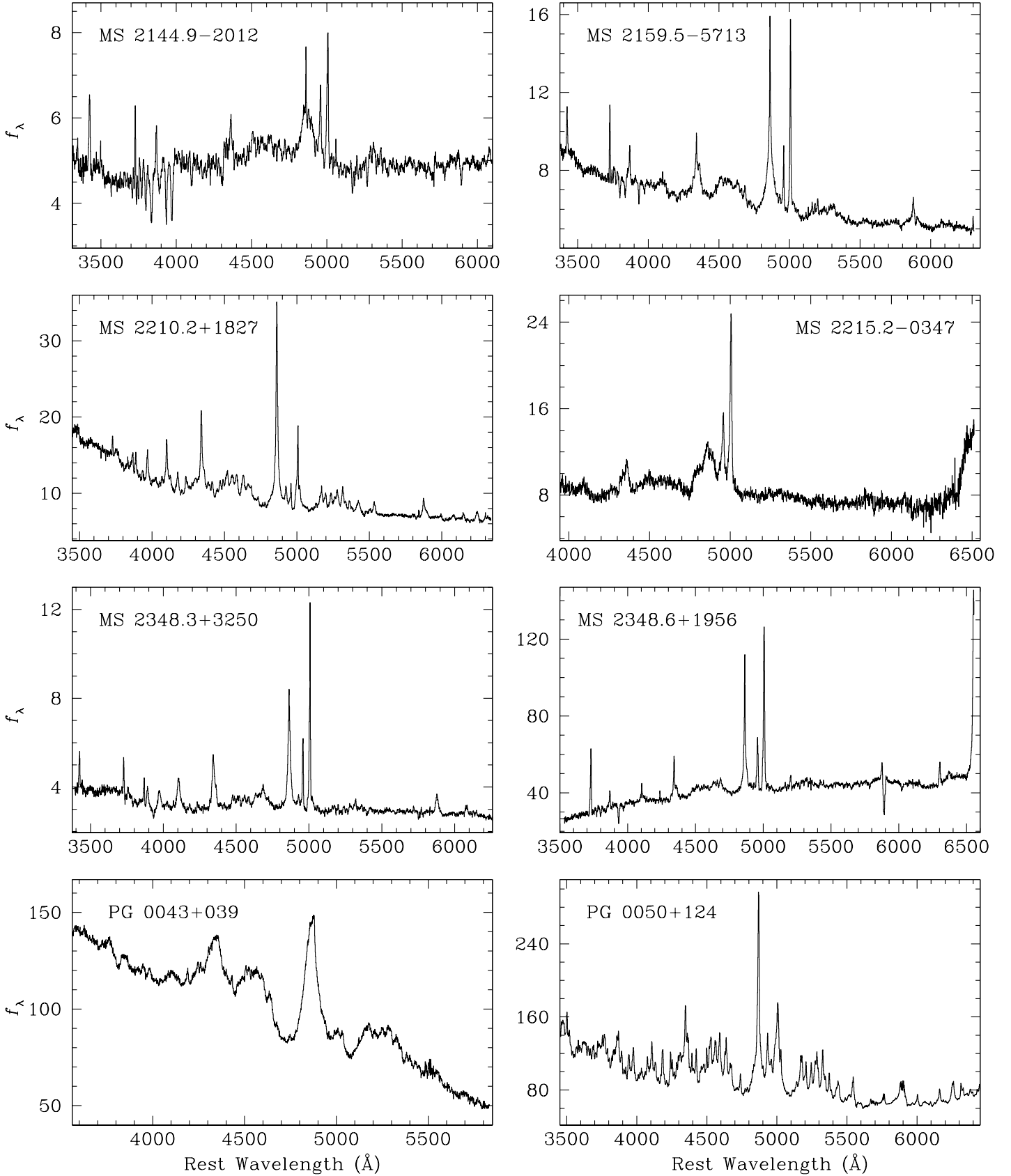


FIG. 1.— Spectral atlas. The ordinate is in units of 10^{-16} erg s^{-1} cm^{-2} \AA^{-1} . Objects marked with “(s)” were smoothed with a 5-pixel boxcar.

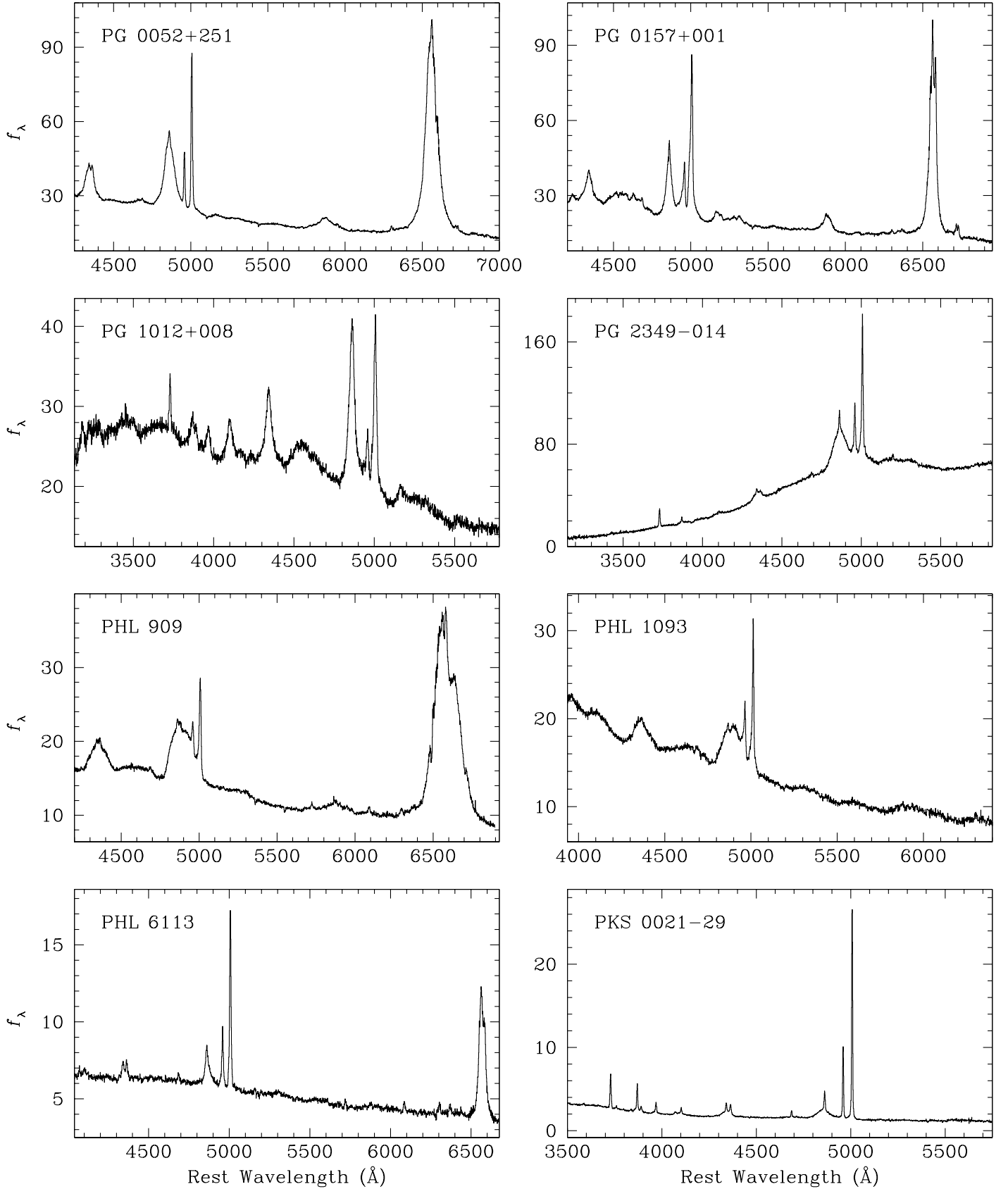


FIG. 1.— Spectral atlas. The ordinate is in units of $10^{-16} \text{ erg s}^{-1} \text{ cm}^{-2} \text{ \AA}^{-1}$. Objects marked with “(s)” were smoothed with a 5-pixel boxcar.

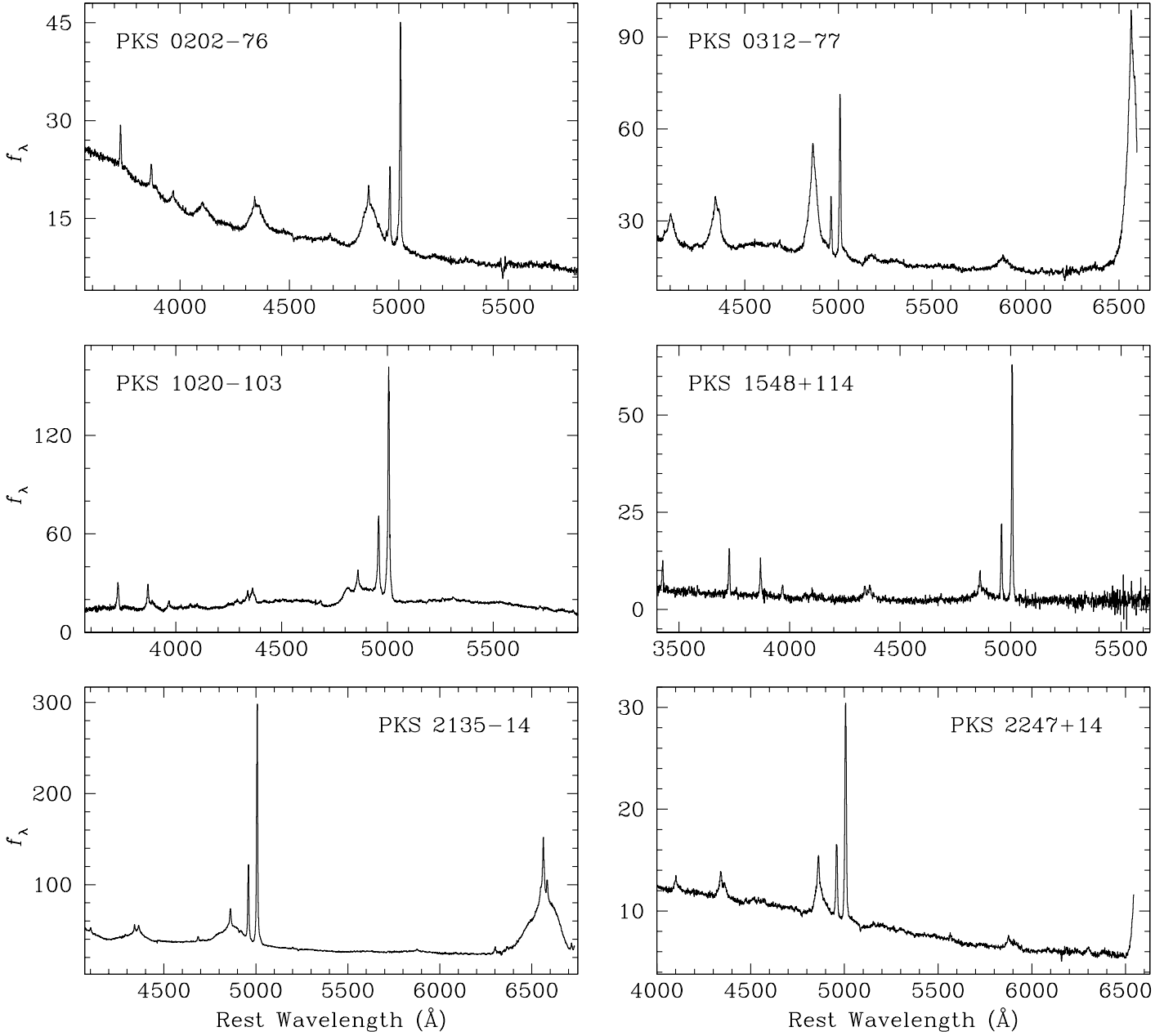


FIG. 1.— Spectral atlas. The ordinate is in units of $10^{-16} \text{ erg s}^{-1} \text{ cm}^{-2} \text{ \AA}^{-1}$. Objects marked with “(s)” were smoothed with a 5-pixel boxcar.

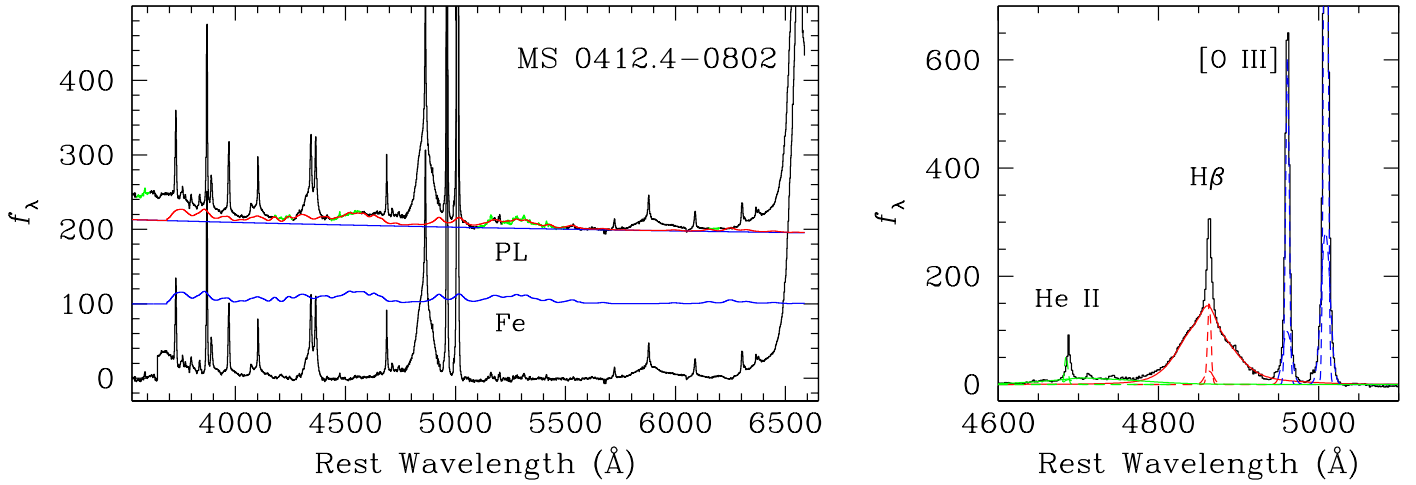


FIG. 2.— Example of spectral decomposition for MS 0412.4–0802. The ordinate is in units of $10^{-17} \text{ erg s}^{-1} \text{ cm}^{-2} \text{ \AA}^{-1}$. The *left* panel shows the original data (*black histograms*), the different components of the continuum fit (*blue lines*; “PL” = power law, “Fe” = iron template), and the final model (*red line*), each offset in the ordinate by a constant, arbitrary amount for clarity. The regions used in the fit are highlighted in *green*. The *bottom* plot shows the residual, pure emission-line spectrum. The *right* panel illustrates our procedure for line fitting for He II (*green*), H β (*red*), and [O III] $\lambda\lambda 4959, 5007$ (*blue*); solid and dashed lines denote broad and narrow components, respectively.

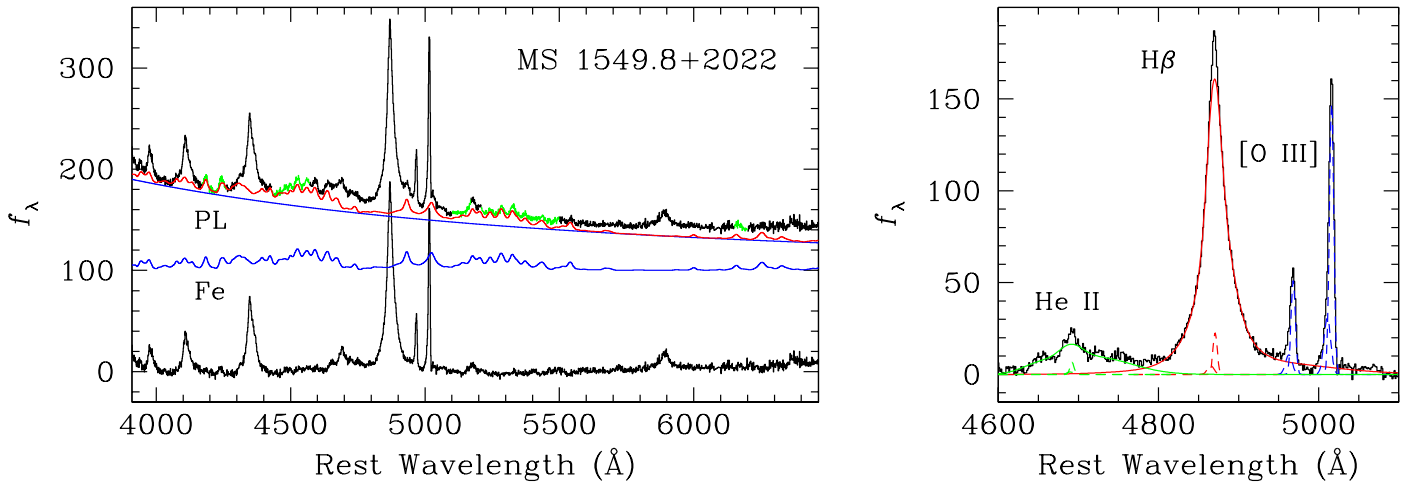


FIG. 3.— Example of spectral decomposition for MS 1549.8+2022; conventions same as in Figure 2.

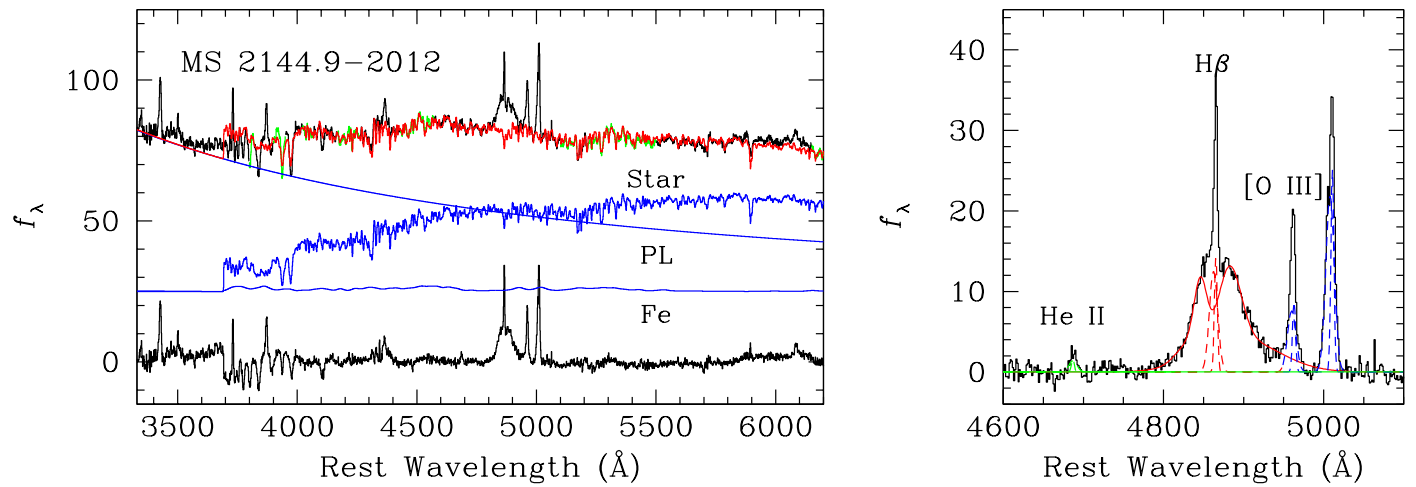


FIG. 4.— Example of spectral decomposition for MS 2144.9-2012; conventions same as in Figure 2, except that the continuum model in this case contains a component for starlight (“Star”) from the host galaxy.

Table 2. Spectral Measurements

Name	S/N	F_{5100}	Star Fraction	β	Fe II Flux	He II _b Flux	He II _n Flux	H β _b Flux	H β _b FWHM	H β _n Flux	[O II] Flux	[O III] Flux	[O III] FWHM	Notes
(1)	(2)	(3)	(4)	(5)	(6)	(7)	(8)	(9)	(10)	(11)	(12)	(13)	(14)	(15)
3C 47	89	-15.41	0.00	-2.25	< -14.28	-14.55	-15.38	-13.60	12886	-14.64	-14.70	-13.65	538	
3C 48	58	-14.61	0.00	-1.87	-12.65	-13.97 :	-14.20	-12.90	3271	-13.90	-13.67	-12.92	1163	
3C 59	100	-14.74	0.00	-0.94	-13.47	-13.53	-14.34	-12.72	10680	-13.93	...	-12.82	365	
3C 93	101	-15.19	0.00	-2.35	-13.90	...	-15.84 :	-13.32	21454	-15.15 :	-14.83	-14.07	600	1
3C 206	97	-15.12	0.00	-1.62	-13.82	...	-15.19	-12.98	5589	-14.63	-14.71	-13.71	752	1
[HB89] 0205+024	163	-14.64	0.00	-1.98	-13.10	-13.28	-14.76	-12.95	1408	-13.64	...	-13.14	397	
[HB89] 0257+024	66	-14.95	0.00	-0.80	-13.53	-13.68	-15.27 :	-13.12	4716	-14.68	...	-13.58	640	
[HB89] 0316-346	56	-14.18	0.00	...	-12.48 :	-12.17	7057	-13.69	-13.78	-13.12	504	2
[HB89] 0450-299	119	-14.69	0.00	-1.67	-12.93	-13.69	-15.03 :	-12.76	1612	-13.90	...	-13.26	584	
[HB89] 0736+017	136	-14.51	0.00	-0.73	-13.11	-13.71	-14.87 :	-12.75	2762	< -14.94	< -15.22	-13.86 :	752 :	
[HB89] 1635+119	86	-15.11	0.00	-1.57	-13.58	-14.09	-15.51	-13.21	6794	-15.29	-15.02	-14.03	252	
[HB89] 2201+315	219	-14.24	0.00	-3.19 :	-12.37 :	-12.96 :	-15.05 :	-12.18	4098	-14.08 :	...	-13.44	752	
[HB89] 2344+184	49	-14.54	0.80	+0.59 :	-13.01 :	< -13.36	-14.90 :	-13.31	7625	-14.09	-13.63	-13.22	286	
HE 1029-1401	282	-13.58	0.00	-2.14	-12.18	-12.67	-14.24 :	-11.50	6589	-13.40	-13.52	-12.54	576	
LBQS 0020+0018	43	-15.88	0.00	-2.34	-14.33	< -14.80	-15.89	-14.16	8368	-15.60	-15.28	-14.69	409	
LBQS 0021-0301	34	-15.67	0.00	-2.39	-13.77	< -14.70	-15.90 :	-13.83	4364	-15.42 :	-15.66	-14.71	716	
LBQS 2214-1903	36	-15.38	0.00	-2.08	-13.51	< -14.62	-15.52 :	-13.56	3493	-14.28	-14.97	-14.35	1011	
MS 0007.1-0231	97	-14.99	0.46	-0.10 :	-13.23	< -14.02	< -14.88	-13.30	6036	-14.83 :	-14.48	-14.20	740	
MS 0039.0-0145	46	-15.60	0.96	-1.55 :	-15.41 :	-14.75	-14.21	-13.87	626	3
MS 0048.8+2907	153	-13.77	0.65	-0.22 :	-12.66 :	< -13.16	-13.81	-12.43	4269	-13.04	-12.96	-12.18	423	
MS 0100.6+0205	35	-15.17	0.00	-1.54	-13.65	< -14.09	-15.30 :	-13.17	6023	-14.70	-14.95	-13.68	489	
MS 0111.9-0132	48	-15.78	0.00	-0.95	-14.01	-14.31	-15.57	-13.80	1574	-15.17	-15.42	-14.27	341	
MS 0135.4+0256	38	-15.46	0.00	-0.94	-13.56	-14.18	-15.70 :	-13.58	1790	-15.24	-15.33	-14.38	198	
MS 0144.2-0055	58	-15.64	0.00	-1.28	-13.84	-14.21	-15.53	-13.63	1368	-14.80	-15.18	-14.09	170	

Table 2—Continued

Name	S/N	F_{5100}	Star Fraction	β	Fe II Flux	He II _b Flux	He II _n Flux	H β _b Flux	H β _b FWHM	H β _n Flux	[O II] Flux	[O III] Flux	[O III] FWHM	Notes
(1)	(2)	(3)	(4)	(5)	(6)	(7)	(8)	(9)	(10)	(11)	(12)	(13)	(14)	(15)
MS 0244.8+1928	77	-14.92	0.00	-1.95	-13.30	-13.77	-15.20 :	-12.81	3831	-14.74	...	-13.73	382	
MS 0321.5-6657	56	-14.62	0.73	-0.31 :	< -13.29	< -13.72	-15.00 :	-13.56	4683	-14.18	-13.90	-13.36	181	
MS 0330.8+0606	71	-15.13	0.72	-1.77 :	-13.66	-14.86 :	< -15.19	-13.50	4848	-14.73	-14.63	-13.97	319	
MS 0340.3+0455	56	-15.11	0.72	-2.15 :	-13.89 :	< -14.10	< -15.19	-16.09 :	4352 :	-14.77	-14.51	-14.29	188	
MS 0412.4-0802	310	-14.99	0.00	-0.27	-13.49	-13.79	-14.41	-12.97	3860	-13.94	-14.10	-12.87	231	
MS 0444.9-1000	41	-15.27	0.75	-1.10 :	-14.00 :	< -14.56	-15.10	-14.00	2123	-14.81	-14.35	-14.06	496	
MS 0457.9+0141	68	-15.32	0.00	-0.53	-14.26 :	-13.94	-15.22	-13.63	2524	-14.75	-14.50	-13.78	390	
MS 0516.6-4609	33	-14.73	0.88	-2.41 :	< -14.80	-14.34	-13.85	-13.58	265	3
MS 0801.9+2129	59	-14.95	0.00	-1.78	-13.18	-14.01	-15.56 :	-13.00	6333	-14.99	-14.77	-13.96	296	
MS 0841.7+1628	40	-15.85	0.00	-1.63	-14.37	-14.52 :	-15.87 :	-13.93	7455	-15.48	-14.98	-14.53	434	
MS 0842.7-0720	54	-15.17	0.00	-1.17	-13.11	-14.37 :	-15.34 :	-13.27	2074	-14.80	-15.14 :	-14.14	449	
MS 0844.9+1836	27	-15.32	0.50	-2.39	-14.24	-14.50 :	< -15.11	-13.89	3073	-14.67	-14.46	-14.39	449	
MS 0849.5+0805	44	-14.78	0.00	-2.44	-13.34	-13.59 :	-14.60	-12.93	2998	-14.19	-13.81	-13.19	376	
MS 0904.4-1505	30	-14.97	0.49	-1.40	-13.48	< -14.37	< -14.76	-13.91	1181	-14.28	-14.46	-13.81	390	
MS 0905.6-0817	30	-15.06	0.63	-0.38 :	-13.64	< -14.00	-15.09	-13.78	4757	-14.39	-14.18	-13.36	154	
MS 0942.8+0950	100	-15.09	0.79	-1.94 :	-13.78	-13.95	-14.60	-13.49	3312	< -15.32	...	-13.92	480	
MS 0944.1+1333	29	-16.09	0.76	+0.18 :	< -16.49	-16.51 :	-15.52	-16.10	169	3
MS 1058.8+1003	88	-14.90	1.00	< -15.11	-14.06	...	-14.08	332	3,4
MS 1108.3+3530	50	-15.30	0.70	-1.51	< -15.45	-14.33	-14.26 :	-13.92	447	3
MS 1110.3+2210	59	-15.57	1.00	-15.84	-15.07	...	-14.38	105	3
MS 1114.4+1801	49	-14.90	1.00	-15.06 :	-14.66	-14.11	-13.97	330	3
MS 1136.5+3413	67	-15.21	0.00	+0.21 :	-13.17	-13.45	-15.26	-13.18	1356	-14.97	...	-13.88	215	
MS 1139.7+1040	24	-15.59	0.00	-1.21	-14.56 :	-14.37 :	-15.78 :	-13.71	5000	-15.30	-15.05	-14.23	206	
MS 1143.5-0411	46	-15.43	0.00	-0.93	-13.65	-14.14	-15.24	-13.52	2945	-14.97	-14.97	-13.92	660	

Table 2—Continued

Name	S/N	F_{5100}	Star Fraction	β	Fe II Flux	He II _b Flux	He II _n Flux	H β _b Flux	H β _b FWHM	H β _n Flux	[O II] Flux	[O III] Flux	[O III] FWHM	Notes
(1)	(2)	(3)	(4)	(5)	(6)	(7)	(8)	(9)	(10)	(11)	(12)	(13)	(14)	(15)
MS 1158.6–0323	89	–14.73	0.24	–1.51	–13.72	–13.70	–14.44	–12.95	2414	–13.86	–13.65	–12.80	165	
MS 1200.1–0330	69	–14.94	0.87	–2.43 :	< –14.99	–14.51	–14.01	–13.87	603	3
MS 1217.0+0700	26	–15.22	0.00	–0.85	–13.26	–14.55 :	< –15.19	–13.36	2024	–14.82	–14.95	–14.42	315	
MS 1220.9+1601	58	–15.55	0.62	–2.19	< –14.37	–14.53 :	< –16.02	–14.27	5590	–14.97	–14.70	–14.83	223	
MS 1232.4+1550	81	–15.21	0.30	–1.66	–13.83	–14.21	–15.18	–13.72	1770	–14.36	–14.45	–13.81	233	
MS 1239.2+3219	26	–15.47	0.74	+0.63 :	< –14.20	–14.79 :	–15.06	–14.32	2062	–14.50	–15.11	–13.58	222	
MS 1242.2+1632	19	–15.20	0.53	–0.87	< –15.04	–14.44	–14.40	–14.96	120	3
MS 1306.1–0115	43	–15.53	0.44	–1.78	–14.16	–14.17	–15.35	–13.96	1843	–15.08	–14.69	–14.09	368	
MS 1322.3+2925	35	–15.56	0.72	–1.46 :	–14.01	–14.38	–15.34	–13.80	1209	–14.78	–15.51 :	–14.47	272	
MS 1334.6+0351	21	–15.76	0.27	...	–14.43	< –14.99	–15.84	–14.72 :	1877 :	–15.41	–15.05	–14.59	201	2
MS 1335.1–3128	18	–15.88	0.62	–1.80	–15.10 :	< –15.10	–16.35 :	–14.37 :	5563 :	–16.81 :	–15.53 :	–14.93	255	
MS 1414.0+0130	36	–15.77	0.60	–3.20	–14.66	–14.74 :	–15.54	–14.16	1865	–14.98	–15.21	–14.46	264	
MS 1414.9+1337	49	–15.68	0.76	–1.32	–15.88 :	–15.21	–15.30	–14.81	208	3,4
MS 1416.3–1257	57	–14.80	0.00	–1.03	–14.20	–13.52	–14.63	–12.51	7530	–13.61	–13.42	–12.83	428	
MS 1426.5+0130	282	–14.14	0.00	–2.54	–12.66	–13.21	–14.64	–12.19	5828	–14.10	–14.27	–13.19	422	
MS 1455.7+2121	37	–15.27	0.67	–1.39	< –13.76	–14.31 :	–15.47 :	–13.85	4175	–14.69	–14.60 :	–14.00	211	
MS 1456.4+2147	60	–15.10	0.00	–1.68	–13.40	–13.94	–14.83	–13.17	1678	–14.01	–13.73	–13.26	168	
MS 1519.8–0633	84	–14.26	0.00	–1.55	–12.45	–13.03	–14.06	–12.38	1319	–13.35	–13.76	–13.00	612	
MS 1545.3+0305	45	–15.22	0.42	–2.65	–13.67	< –14.20	–15.07	–13.58	5179	–14.55	–14.37	–13.72	438	
MS 1549.8+2022	56	–15.25	0.00	–2.00	–13.45	–13.80	–15.25	–13.11	1865	–14.70	...	–13.87	303	
MS 1846.5–7857	112	–13.72	0.38	–0.35	–12.22	< –13.28	–14.16	–11.91	3480	–13.58	–13.24	–12.42	242	
MS 2039.5–0107	50	–15.69	0.00	–0.59	–13.95	–14.38	–15.60	–14.14	1274	–14.85	–14.92	–14.34	238	
MS 2128.3+0349	135	–14.88	0.00	–1.67	–13.51	–13.40	–14.85	–12.74	3053	–14.23	–13.98	–13.19	252	
MS 2141.2+1730	105	–14.48	0.00	–2.11	–13.00	–13.19	< –14.34	–12.71	4884	–14.69 :	...	–13.49	887	
MS 2144.9–2012	74	–15.28	0.50	–1.15	–14.34	< –14.96	–15.61	–13.98	4339	–14.64	–14.88	–14.38	369	

Table 2—Continued

Name	S/N	F_{5100}	Star Fraction	β	Fe II Flux	He II _b Flux	He II _n Flux	H β _b Flux	H β _b FWHM	H β _n Flux	[O II] Flux	[O III] Flux	[O III] FWHM	Notes
(1)	(2)	(3)	(4)	(5)	(6)	(7)	(8)	(9)	(10)	(11)	(12)	(13)	(14)	(15)
MS 2159.5–5713	103	–15.22	0.38	–2.01	–13.65	< –14.99	–15.19	–13.68	2437	–14.30	–14.60	–14.11	255	
MS 2210.2+1827	111	–15.04	0.00	–1.32	–13.18	–14.16	–14.98	–13.39	1257	–13.84	–14.89	–14.09	325	
MS 2215.2–0347	29	–14.98	0.00	–0.64	–13.18	< –13.80	–15.02 :	–13.08	10023	–14.74	...	–13.53	578	
MS 2348.3+3250	53	–15.47	0.31	–1.43	–14.12	–14.30	–15.29	–13.85	1290	–14.96	–14.92	–14.10	320	
MS 2348.6+1956	109	–14.29	0.36	+0.31	–12.89	–13.52	–14.27	–13.01	1255	–13.35	–13.43	–12.95	499	
PG 0043+039	131	–14.09	0.00	–1.72	–12.19	< –13.32	< –13.91	–12.31	4684	< –13.89	–15.08 :	< –13.88	...	5
PG 0050+124	351	–14.02	0.00	–1.23	–11.94	< –14.03	< –13.85	–12.25	758	–13.12	–14.09	–12.56	1679	
PG 0052+251	164	–14.62	0.00	–2.54	–13.38	–13.77	–14.97 :	–12.43	4864	–14.19	...	–13.12	527	
PG 0157+001	111	–14.68	0.00	–2.04	–12.98	–13.56	–14.22	–12.92	2739	–13.71	...	–12.90	762	
PG 1012+008	52	–14.70	0.00	...	–13.12	–14.03 :	< –14.62	–12.97	2479	–14.38	–14.11	–13.29	1141	2
PG 2349–014	128	–14.15	0.00	...	–13.50 :	< –13.50	< –14.56	–12.36 :	6642 :	–13.66	–13.92	–12.82	519	2
PHL 909	145	–14.81	0.00	–1.32	–13.14	–13.51	–15.29 :	–12.75	10736	–14.63	...	–13.68	647	
PHL 1093	113	–14.85	0.00	–2.04	–13.52	–13.83	–15.11	–13.05 :	8745	–14.89	...	–13.67	369	
PHL 6113	87	–15.22	0.00	–1.25	–14.19	–14.36 :	–15.22	–13.79	2594	–14.96	...	–13.84	481	
PKS 0021–29	46	–15.86	0.00	–1.68	< –14.43	–14.82 :	–15.29	–13.92	4264	–14.81	–14.52	–13.74	221	
PKS 0202–76	76	–14.99	0.00	–2.48	–13.54	–14.23	–15.27	–13.07	5146	–14.56	–14.32	–13.51	251	
PKS 0312–77	79	–14.66	0.00	–1.66	–13.18	–13.38	–14.93 :	–12.50	3112	–14.14	...	–13.26	367	
PKS 1020–103	57	–14.67	0.00	+0.96 :	–12.74 :	< –13.74	–14.77	–12.66	10121	–14.07	–13.79	–12.79	442	
PKS 1548+114	5	–15.60	0.00	–1.65	< –13.23	< –13.66	–14.92 :	–13.45	4794	–14.36	–14.07	–13.31	225	
PKS 2135–14	121	–14.44	0.00	–1.64	–13.55	–13.16	–14.31	–12.37	8895	–13.76	...	–12.61	332	
PKS 2247+14	111	–15.02	0.00	–1.62	–13.06	< –14.60	< –15.29	–13.71	2973	–14.51	...	–13.58	472	

Note. — Col. (1): Object name. Col. (2): Signal-to-noise ratio per pixel at 5100 Å. Col. (3): Logarithm of the flux density at 5100 Å, in units of $\text{erg s}^{-1} \text{cm}^{-2} \text{Å}^{-1}$. Col. (4): Starlight contribution to the total flux density at 5100 Å. Col. (5): Spectral index of the power-law component, defined such that $f_\lambda \propto \lambda^\beta$. Col. (6): Flux of Fe II $\lambda 4570$. Col. (7): Flux of broad He II $\lambda 4686$. Col. (8): Flux of narrow He II $\lambda 4686$. Col. (9): Flux of the broad H β . Col. (10): FWHM of the broad H β . Col. (11): Flux of narrow H β . Col. (12): Flux of [O II] $\lambda 3727$. Col. (13): Flux of [O III] $\lambda 5007$. Col. (14): FWHM of [O III] $\lambda 5007$. Col. (15): Notes: (1) Impossible to measure broad He II because broad H β is very broad and asymmetric. (2) Spectral shape distorted by slit losses due to atmospheric differential refraction. (3) Narrow-line source; see Section 5. (4) Broad H α emission present in Sloan Digital Sky Survey spectrum. (5) Upper limit on the narrow lines assuming FWHM = 500 km s^{-1} . All fluxes, in $\text{erg s}^{-1} \text{cm}^{-2}$, are on a logarithmic scale; typical uncertainties are 35% for the broad lines and 10% for the narrow lines, but in the worst cases (indicated by a colon) may be a factor of 2–3 larger. All FWHM are in units of km s^{-1} and have been corrected for instrumental resolution; typical uncertainties are 10% for the broad lines and 5% for the narrow lines, but may be a factor of 2–3 larger for entries flagged with a colon.

4. MEASUREMENTS

4.1. *Spectral Decomposition*

Although the primary purpose of this paper is to present the spectral atlas of our database, we also measure a number of basic spectral parameters for the continuum and strong emission lines commonly used by the AGN community. Our own forthcoming host galaxy analyses will draw heavily from this database. These measurements are summarized in Table 2. Because of our wavelength coverage, we concentrate on the following emission lines: [O II] $\lambda 3727$, Fe II $\lambda 4570$, He II $\lambda 4686$, H β $\lambda 4861$, and [O III] $\lambda\lambda 4959, 5007$. Our approach closely follows that of Greene & Ho (2005b) and Kim et al. (2006), which the reader can consult for more details. Here we briefly summarize a few key points.

The optical continuum is a complex mixture of several components, which must be modeled and subtracted prior to measuring the emission lines. We decompose the continuum using a model consisting of up to three components: (1) starlight from the host galaxy, (2) featureless continuum from the AGN, and (3) Fe II emission. We do not account for internal extinction, as there is no unambiguous, universally accepted method of doing so this type of data. We include a galaxy component only if the observed spectrum contains a sufficiently strong starlight component. Following Kim et al. (2006), we require that the equivalent width of the Ca II K line exceed 1.5 Å; this corresponds roughly to a starlight contribution of $\gtrsim 10\%$ to the local continuum. The galaxy continuum is modeled by a linear combination of a G-type and a K-type giant, which, in most cases, suffices to match host galaxies with a predominantly evolved stellar population. Some sources show a significant contribution from intermediate-age stars, as evidenced by the presence of strong higher-order Balmer lines (e.g., MS 1220.9+1601, MS 2144.9–2012, and MS 2159.5–5713; see Figure 1). For these cases adding an additional A-type star does an adequate job of representing the young population. Over the limited wavelength range under consideration, the featureless nonstellar continuum can be approximated using a single power-law function. In a few cases the AGN continuum is slightly more complex, and a better fit can be achieved using the sum of two power-law functions. Finally, blends of broad Fe II transitions form a complicated pseudocontinuum that affects significant portions of the ultraviolet and optical spectrum of most type 1 AGNs. Following standard practice, we model the Fe II component using a scaled and broadened Fe template derived from observations of the narrow-line Seyfert 1 (NLS1) galaxy I Zw 1 (Boroson & Green 1992); the Fe template was kindly provided by T. Boroson. As in Hu et al. (2008a, 2008b), we allow both the width and the radial velocity of the Fe template to be free parameters in the fit, because the kinematics of Fe II need not be identical to those of broad H β . The Boroson & Green Fe template, unfortunately, does not extend below 3700 Å. Because of this, we do not bother to include the Balmer continuum in the continuum model, since the fit below 3700 Å should not be trusted anyway.

The fit is performed over the following spectral regions devoid of strong emission lines: 3900–3950, 4020–4070, 4170–4260, 4430–4570, 5100–5170, 5210–5500, and 6150–6200 Å. In practice, however, we adjust the exact fitting regions to achieve the best fit. Figures 2 and 3 give examples of two sources for which the AGN is sufficiently strong that the continuum can be modeled with just the power-law and Fe com-

ponents; in the case shown in Figure 4, the stellar component clearly must be included too.

After continuum subtraction, we fit the residual spectrum in order to measure the parameters of several prominent emission lines. For the narrow emission lines, we follow the same procedure used by Kim et al. (2006). If the [S II] $\lambda\lambda 6716, 6731$ doublet is included in the bandpass and the S/N is adequate, we use the profile of [S II] to constraint [N II] $\lambda\lambda 6548, 6583$ and the narrow component of H α and H β . However, in the majority of the objects [S II] lies outside of our spectral coverage. In this situation we have no choice but to rely on [O III] as a template for the narrow lines. As in Greene & Ho (2005a), we fit each of the lines of the [O III] $\lambda\lambda 4959, 5007$ doublet with one or two Gaussians, depending on whether they show an extended or asymmetric wing. With the profile of the narrow component thus constrained, we fit the broad component of the permitted lines using as many Gaussian components as necessary to achieve an acceptable fit (typically only 2–3 suffice).

The He II $\lambda 4686$ emission line, while diagnostically important, is challenging to measure accurately because it is much weaker than H β and because it lies on the shoulder of the strong Fe II $\lambda 4570$ blend to the blue and H β to the red. We treat He II in the same manner as H β , using [O III] as a template for its narrow component, and a multi-Gaussian model for the broad component. If either component is undetected, we set an upper limit based on 3 times the rms noise of the local continuum and an assumed velocity width; for the narrow component, we use the [O III] profile, whereas the broad H β profile is used for the broad component.

As in previous studies (e.g., Boroson & Green 1992; Marziani et al. 2003), we select the prominent Fe II blend at 4570 Å to represent the strength of the optical Fe emission. The flux of the feature is integrated over the region 4434–4684 Å. If undetected, we calculate the 3σ upper limit from the rms noise over this region.

Finally, we give measurements for [O II] $\lambda 3727$, whose strength provides constraints on the ongoing star formation rate in AGNs (Ho 2005). As in Kim et al. (2006; see also Kuraszekiewicz et al. 2000), we measure the line strength by simply fitting a single Gaussian with respect to the local continuum near 3700 Å. This procedure suffices because the [O II] doublet remains unresolved at the relatively low resolution of our observations, and measuring the line locally bypasses the complications of the poor continuum fits in the blue part of the spectra. Upper limits are set using the local rms noise and the velocity width of [O III].

The velocity widths of [O III] listed in Table 2 pertain to the FWHM of the final model for the entire line profile, and have been corrected for instrumental resolution by subtracting it in quadrature.

4.2. *Uncertainties*

Robust uncertainties are notoriously difficult to derive for spectral measurements of the type presented above. In almost all cases the formal error bars from the fits underestimate the true errors, which are dominated by systematic uncertainties in the myriad assumptions that enter into the complicated fits. For this reason we resist assigning specific error bars to the entries in Table 2. Nevertheless, based on past experience with analysis of this type (e.g., Ho et al. 1997; Greene & Ho 2005b; Kim et al. 2006; Hu et al. 2008a, 2008b), in the notes to Table 2 we give some rough estimates of the typical uncertainties involved.

5. GENERAL PROPERTIES OF THE EMSS AGNS

As the EMSS AGNs have never been analyzed spectroscopically in a quantitative manner, and our survey contains a significant fraction (80%) of the sample studied by Schade et al. (2000), we will give a few general statistics on the spectroscopic properties of these objects. The EMSS was conducted in the 0.3–3.5 keV band and, as such, is expected to be biased toward sources that are bright in soft X-rays. Because of their strong soft X-ray emission (e.g., Boller et al. 1996; Grupe et al. 2004), NLS1s should be overrepresented in AGNs selected on the basis of their soft X-ray emission compared to selection in other wavelengths (e.g., optical). This is especially true because of the relatively low luminosities probed by the EMSS. We confirm this expectation. Among the 51 EMSS sources with detected broad $H\beta$ emission, 33% have $H\beta$ FWHM < 2000 km s⁻¹, the conventional linewidth criterion for NLS1s. This fraction increases to 47% if we relax the (somewhat arbitrary) FWHM cutoff to 2500 km s⁻¹. As expected from previous studies, these sources tend to show relatively weak [O III] lines but prominent Fe II emission. By comparison, within the sample of ~ 8500 low-redshift ($z \lesssim 0.35$), optically selected type 1 AGNs studied by Greene & Ho (2007), the fraction of sources with $H\alpha$ FWHM < 2000 km s⁻¹ is 24%, increasing to 40% for FWHM < 2500 km s⁻¹. [To zeroth order, broad $H\alpha$ and $H\beta$ have similar line profiles (Greene & Ho 2005b).]

In terms of their luminosities, all of the EMSS sources should be regarded as Seyferts rather than quasars. Their broad $H\beta$ luminosities range from $\sim 10^{39}$ to 10^{43} erg s⁻¹, with a median value of $\sim 10^{42}$ erg s⁻¹; using a standard conversion from line to continuum luminosity (Greene & Ho 2005b), this corresponds to a median absolute magnitude of only $M_B \approx -19$, roughly near the knee of the luminosity function of local Seyfert galaxies (see Figure 8 in Ho 2008). Despite their modest luminosities, as discussed in M. Kim et al. (in preparation), the EMSS sources are radiating at a healthy fraction of their Eddington rates ($L_{\text{bol}}/L_{\text{Edd}} \approx 0.01 - 1$) because their black hole masses are relatively low ($M_{\text{BH}} \approx 10^6 - 10^8 M_{\odot}$), consistent with their hosts being mostly spiral galaxies (Schade et al. 2000).

While our original intent was to observe type 1 AGNs for which we can estimate black hole masses, 10 objects from the EMSS sample turn out to reveal only narrow emission lines in our spectral range (see Table 2). Of these, two have Sloan Digital Sky Survey spectra that extend further to the red than our spectra. MS 1058.8+1003 shows a double-peaked broad $H\alpha$ line, and the relative intensities of its narrow lines qualify it as a low-ionization nuclear emission-line region; following the nomenclature of Ho et al. (1997), it should be classified as a LINER 1.9. MS 1414.9+1337 also has weak broad $H\alpha$ emission, but its higher-ionization narrow-line spectrum qualifies it as a Seyfert 1.9. As for the rest, only three (MS 0039.0–0145, 0516.6–4609, and 1110.3+2210) appear to be genuine type 2 Seyferts, as judged by their large [O III]/ $H\beta$ ratios and, for the latter two, detection of relatively strong [O I] $\lambda 6300$. Without the help of the diagnostic lines near $H\alpha$ (see Ho 2008), the physical nature of the remaining five objects — MS 0944.1+1333, 1108.3+3530, 1114.4+1801, 1200.1–0330, and 1242.2+1632 — is somewhat ambiguous. But judging from the relative strengths of [O II], [O III], and $H\beta$, we suspect that these sources are not powered by AGNs but rather by star formation.

6. SUMMARY

We have used the Magellan 6.5 m Clay Telescope to obtain moderate-resolution ($R \approx 1200 - 1600$) optical spectra covering the rest-frame region $\sim 3600 - 6000$ Å for a sample of 94 low-redshift ($z \lesssim 0.5$) type 1 AGNs. Although some of the objects are well-known sources, the majority do not have reliable spectroscopy in the literature that can be used to estimate black hole masses from their broad emission lines. We pay special attention to the sample of soft X-ray-selected (EMSS) AGNs with good-quality *HST* images studied by Schade et al. (2000). Eight of the sources turn out to be narrow-line objects that were previously misclassified as broad-line AGNs; of these only three are Seyfert 2 galaxies and the rest appear to be powered by stars. We present a spectral atlas of our sample and basic measurements for a number of prominent, commonly used emission lines. These data will be used in a separate paper aimed at studying the relationship between black hole mass and the properties of their host galaxies.

This work was supported by the Carnegie Institution for Science and by NASA grants HST-AR-10969.03-A and HST-GO-10428.11-A from the Space Telescope Science Institute (operated by AURA, Inc., under NASA contract NAS5-26555). M. K. was supported by the Korea Science and Engineering Foundation (KOSEF) grant No. 2009-0063616, funded by the Korean government (MEST). We made use of the NASA/IPAC Extragalactic Database (NED), which is operated by the Jet Propulsion Laboratory, California Institute of Technology, under contract with NASA. We thank Todd Boroson for making available his Fe template spectrum. We are grateful to an anonymous referee for a constructive review of this work.

REFERENCES

- Baldwin, J. A., & Stone, R. P. S. 1984, *MNRAS*, 206, 241
Bentz, M. C., Peterson, B. M., Netzer, H., Pogge, R. W., & Vestergaard, M. 2009, *ApJ*, 697, 160
Boller, T., Brandt, W. N., & Fink, H. 1996, *A&A*, 305, 53
Boroson, T. A., & Green, R. F. 1992, *ApJS*, 80, 109
Cardelli, J. A., Clayton, G. C., & Mathis, J. S. 1989, *ApJ*, 345, 245
Dunlop, J. S., McLure, R. J., Kukula, M. J., Baum, S. A., O'Dea, C. P., & Hughes, D. H. 2003, *MNRAS*, 340, 1095
Gioia, I. M., Maccacaro, T., Schild, R. E., Wolter, A., Stocke, J. T., Morris, S. L., & Henry, J. P. 1990, *ApJS*, 72, 567
Greene, J. E., & Ho, L. C. 2005a, *ApJ*, 627, 721
Greene, J. E., & Ho, L. C. 2005b, *ApJ*, 630, 122
Greene, J. E., & Ho, L. C. 2007, *ApJ*, 667, 131
Grupe, D., Wills, B. J., Leighly, K. M., & Meusinger, H. 2004, *AJ*, 127, 156
Hamilton, T. S., Casertano, S., & Turnshek, D. A. 2002, *ApJ*, 576, 61
Ho, L. C. 2004, ed., *Carnegie Observatories Astrophysics Series, Vol. 1: Coevolution of Black Holes and Galaxies* (Cambridge: Cambridge Univ. Press)
Ho, L. C. 2005, *ApJ*, 629, 680
Ho, L. C. 2008, *ARA&A*, 46, 475
Ho, L. C., Filippenko, A. V., & Sargent, W. L. W. 1997, *ApJS*, 112, 315
Horne, K. 1986, *PASP*, 98, 609
Hu, C., Wang, J.-M., Ho, L. C., Chen, Y.-M., Bian, W.-H., & Xue, S.-J. 2008a, *ApJ*, 683, L115
Hu, C., Wang, J.-M., Ho, L. C., Chen, Y.-M., Zhang, H.-T., Bian, W.-H., & Xue, S.-J. 2008b, *ApJ*, 687, 78
Kaspi, S., Maoz, D., Netzer, H., Peterson, B. M., Vestergaard, M., & Jannuzi, B. T. 2005, *ApJ*, 629, 61
Kaspi, S., Smith, P. S., Netzer, H., Maoz, D., Jannuzi, B. T., & Giveon, U. 2000, *ApJ*, 533, 631
Kim, M., Ho, L. C., & Im, M. 2006, *ApJ*, 642, 702
Kim, M., Ho, L. C., Peng, C. Y., Barth, A. J., Im, M., Martini, P., & Nelson, C. H. 2008, *ApJ*, 687, 767
Kim, M., Ho, L. C., Peng, C. Y., & Im, M. 2007, *ApJ*, 658, 107
Kuraszkiewicz, J., Wilkes, B., Brandt, W. N., & Vestergaard, M. 2000, *ApJ*, 542, 631
Marziani, P., Sulentic, J. W., Zamorani, R., Calvani, M., Dultzin-Hacyan, D., Bachev, R., & Zwitter, T. 2003, *ApJS*, 145, 199
McLure, R. J., & Jarvis, M. J. 2002, *MNRAS*, 337, 109
Netzer, H., Shemmer, O., Maiolino, R., Oliva, E., Croom, S., Corbett, E., & di Fabrizio, L. 2004, *ApJ*, 614, 558
Schade, D. J., Boyle, B. J., & Letawsky, M. 2000, *MNRAS*, 315, 498
Schlegel, D. J., Finkbeiner, D. P., & Davis, M. 1998, *ApJ*, 500, 525
Spergel, D. N., et al. 2003, *ApJS*, 148, 175
Stocke, J. T., Morris, S. L., Gioia, I. M., Maccacaro, T., Schild, R., Wolter, A., Fleming, T., & Henry, J. P. 1991, *ApJS*, 76, 813
Stone, R. P. S., & Baldwin, J. A. 1983, *MNRAS*, 204, 347
van Dokkum, P. G. 2001, *PASP*, 113, 1420
Vestergaard, M. 2002, *ApJ*, 571, 733